Last revised October 24, 2001

Study on Acceptances and Resolutions of the H1 VFPS Detector

Addendum to proposal DESY PRC 01/00

H1 Collaboration

Abstract

The acceptance and resolutions of the proposed *Very Forward Proton Spectrometer* (VFPS) are discussed. New studies of the physics potential of the device are described. The overall status of the project is presented.

1 Introduction

The discovery of a large fraction of diffractive processes in DIS at low x and the detailed measurements of such processes is generally recognised to be one of the major successes of the HERA I programme. HERA kinematics are particularly favourable for the study of the photon dissociation $ep \to eXp$ and quasi-elastic vector meson (V) production $ep \to eVp$ processes, since the asymmetric beam configurations result in the system X being well contained in the main detectors. Although many detailed measurements have already been made,[1] there is still plenty of scope for further more precise measurements and investigations of new exclusive channels. It is essential that diffraction remains an integral part of the physics programme at HERA II, so that this unique opportunity to answer fundamental questions in hadronic physics and QCD is not missed. The H1 Very Forward proton Spectrometer (VFPS) offers the opportunity to take advantage of the high luminosity available at HERA II to continue studies of diffraction.

The physics topics which can be studied with the VFPS spectrometer have already been described in [1]. Furthermore, acceptance calculations for particular processes [2] as well as background studies [3] have been added to the proposal as addenda. In all these studies the beam transport description was based on linear beam optics. In order to improve the understanding of how accurately the physical parameters $x_{I\!P}$, t and ϕ can be reconstructed from the spectrometer data, the beam transport description has now been refined. In this new description, the reconstruction of the physical parameters becomes more complicated. Although the

[1] At the time of writing, H1 and ZEUS have published 59 papers on diffraction in refereed journals.

acceptances are unaffected, the resolutions on the physical parameters found with the current reconstruction methods have changed as described in detail below.

In section 2 the new beam transport description is outlined. In section 3 the resolutions on the physical parameters $x_{I\!P}$, t and ϕ are shown, the precision with which the slope parameter b of the t distribution can be extracted is estimated and the detector position calibration is briefly addressed. In the previous notes, the potential of the VFPS spectrometer as a triggering device was not addressed. This issue is discussed in section 4 of this document. Further details of the physics potential of the VFPS that were not covered in previous documents are reviewed in section 5. Finally, in section 6, the status of the VFPS is briefly summarized from the technical point of view.

2 Status of Transport Calculation and Acceptances

In the beam transport calculation, now used for detector acceptance and resolutions estimates, all details regarding the beam pipe and the machine lattice are taken into account. More specifically the following items are included:

1. a complete description of the beam pipe geometry from the interaction point up to the VFPS location at 220 m as shown in fig. 1,
2. the positions and tilts of all the proton beam dipole and quadrupole magnets,
3. the beam-kick, displacing the nominal beam in the interval [150 m, 250 m] to avoid a beampipe acceptance limitation otherwise encountered,
4. the effect of sextupole magnets which technically are accounted for in the simulation by introducing a quadrupole field depending on the transverse distance from the sextupole axis and
5. the beam divergence of both the proton and electron beam at the interaction vertex as well as smearing of the interaction vertex location (see [2]).

In the VFPS proposal [1] a linear beam optics calculation was used in which the relation between the position x and the slope $x' = dx/ds$ of the proton at the VFPS location are related to the scattering angle θ_x and the fractional proton energy loss $x_{I\!P}$ at the H1 interaction point through the following matrix equation:

$$\begin{pmatrix} x \\ x' \end{pmatrix} = \begin{pmatrix} T_x & D_x \\ T'_x & D'_x \end{pmatrix} \cdot \begin{pmatrix} \theta_x \\ x_{I\!P} \end{pmatrix} \tag{1}$$

where T_x, T'_x, D_x and D'_x are energy-independent transport matrix elements which where calculated from lists of optical functions provided by HERA. A similar matrix equation holds for the vertical coordinate y.

The beam optics calculation now takes all the effects listed above into account. The transport matrix elements are calculated using the dipole and quadrupole magnet strengths. To properly

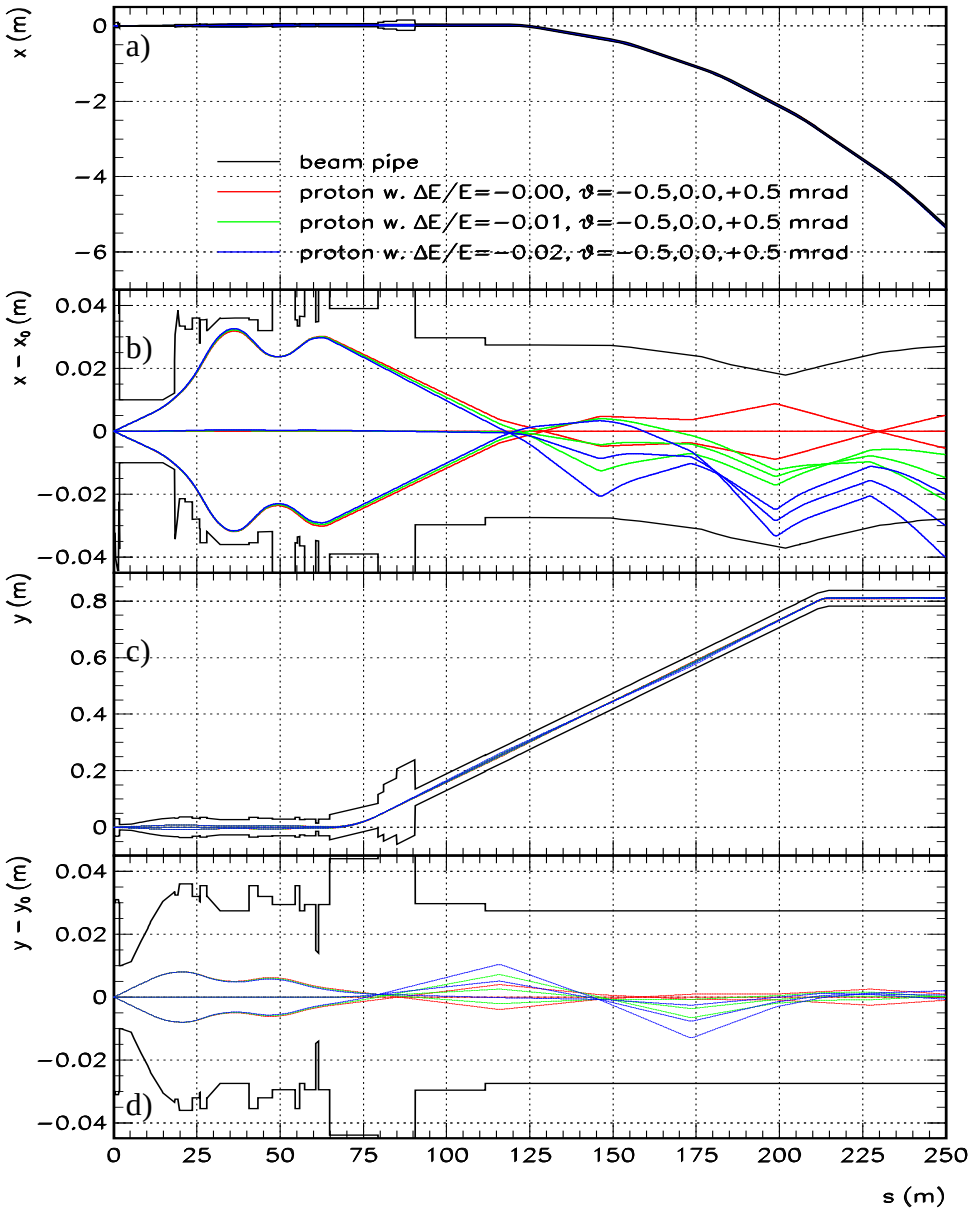

Figure 1: Horizontal and vertical projection of the beam pipe: a) x-projection of the proton beam pipe with respect to the absolute H1 coordinate system; b) x-projection of the beam pipe relative to the nominal beam position; c) y-projection of the proton beam pipe with respect to the absolute H1 coordinate system and d) y-projection of the beam pipe relative to the nominal beam position. Coloured lines show proton trajectories for given proton energy losses and emission angles.

account for off-momentum scattered protons, to all orders of $\Delta E/E$ $(\equiv -x_{I\!P})$ the magnet field strengths are scaled with a E_p/E'_p factor, where E_p and E'_p are the beam and scattered proton energies respectively and $x_{I\!P} = 1 - E'_p/E_p$. For the tracking of particles through the magnets the true direction of the magnet axis (originally assumed to be parallel to the beam axis) is taken into account. This is important as for instance off-centered quadrupoles simulate the effect of a dipole magnet which in turn influences the energy dispersion of the particle. A consequence of the inclusion of these elements is that the transport matrix elements are now energy dependent. The energy dependence of the transport matrix elements T_x, T_y, the dispersion D_x and the derivative of the dispersion D'_x are shown in fig. 2. As can be seen the effect cannot be neglected. As the sextupole magnets might have a compensating effect, those magnets were also included as described in item 4) above. The consequence of this inclusion is not only that the matrix elements and the dispersion are energy dependent, but also that they become functions of the transverse distance to the nominal beam. The global effect of these non-linearities are shown by the coloured lines in the (x, x') and (y, y') plots, (see fig. 3). These figures show the positions and angles of a particle at a z position located half way in between the two Roman pots for particles produced at specified θ_x, θ_y and $x_{I\!P}$, where θ_x and θ_y are the particle emission angles at the vertex. The dotted grid shows the same correlations for the linear beam optics which were used in the proposal [1]. As can be seen, the dotted grid in the (x, x') plot for the linear beam beam optics changes to a much more complex shape for the new calculations. For example, particles emitted at large θ_x are mapped into a small region in the (x, x') plane with the consequence that these θ_x angles can hardly be resolved.

In the calculation for linear beam optics, the χ^2 minimization between the calculated and measured positions and slopes in the Roman pots leads to a system of linear equations from which the physical parameters $x_{I\!P}$, t and ϕ (equivalently $x_{I\!P}$, θ_x and θ_y) can be extracted. In the new framework, the χ^2 minimization results in a non-linear set of equations. The physical parameters are obtained from an iterative minimization procedure (MINUIT). From a practical point of view and at variance with the previous (linear) method, one has to worry about ambiguous results and possible dependences of the results on the assumed starting values of the extracted parameters for the minimisation procedure.

To study the beam pipe and detector acceptance with the new calculations, we have generated events with flat distributions in $x_{I\!P}$ and t in the ranges $0.004 < x_{I\!P} < 0.04$ and $0 < |t| < 1\ \mathrm{GeV}^2$ and passed the scattered protons through the simulation of the forward beamline with the updated beam transport calculation. Fig. 4 shows the acceptance resulting from the aperture of the proton beam pipe as a function of pairs of the kinematical variables. The acceptance of the VFPS depends on how close to the beam it is possible to place the detectors. Fig. 5 shows the acceptance for an example situation in which the detectors are conservatively positioned 3 mm away from the beam, in order to avoid large rates of background tracks from a possible coasting beam component in HERA. Comparison of fig. 4 and fig. 5 reveals that the acceptance in t and the limit at large $x_{I\!P}$ are defined by the beam pipe aperture, while the lower limit of $x_{I\!P}$ that can be reached is directly related to the closest possible approach to the beam.

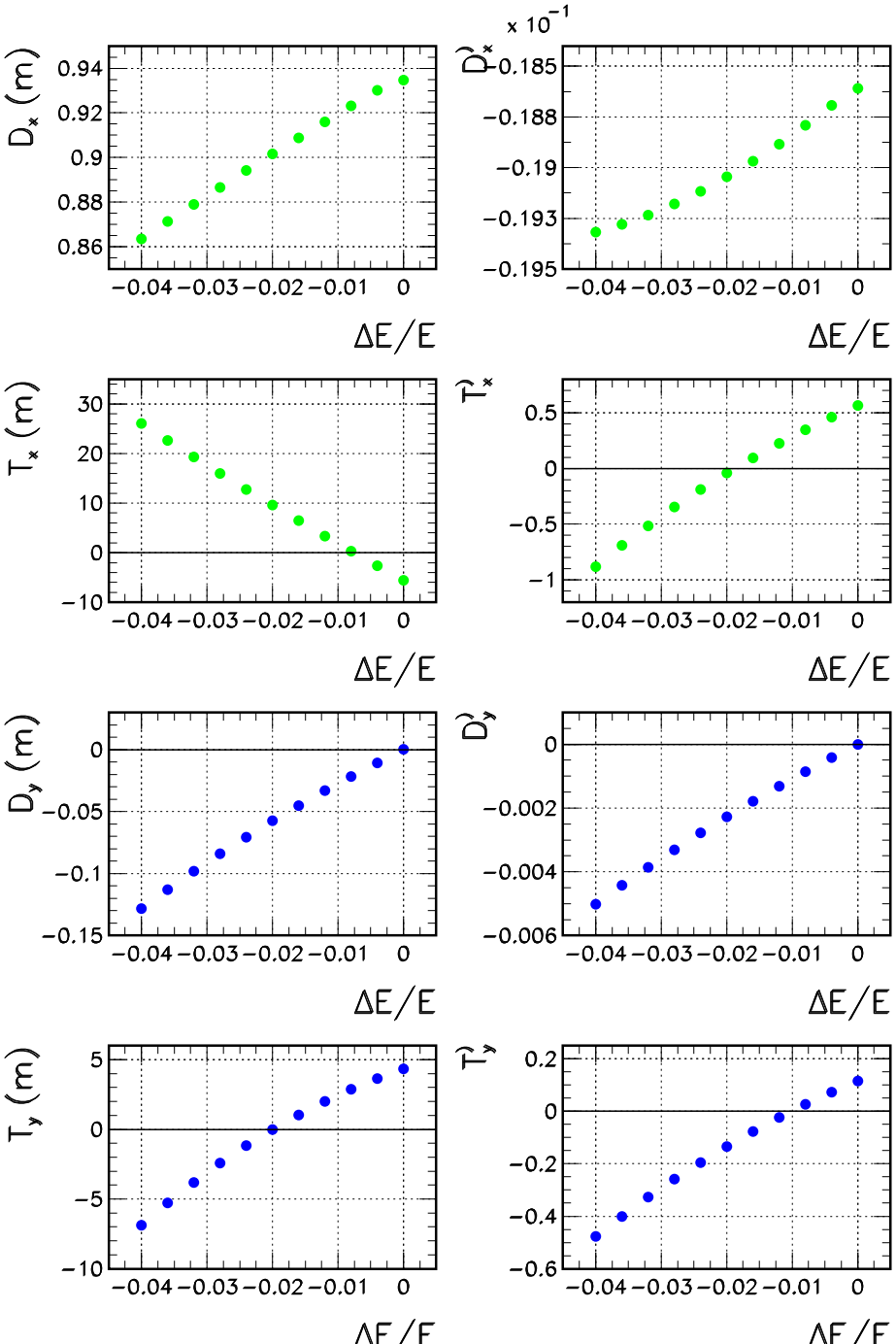

Figure 2: The transport matrix elements T_x, T_y and the dispersions D_x, D_y as defined in equation 1, shown as functions of the relative energy change between the beam and scattered protons $\Delta E/E$ (the effects of sextupole fields are not included).

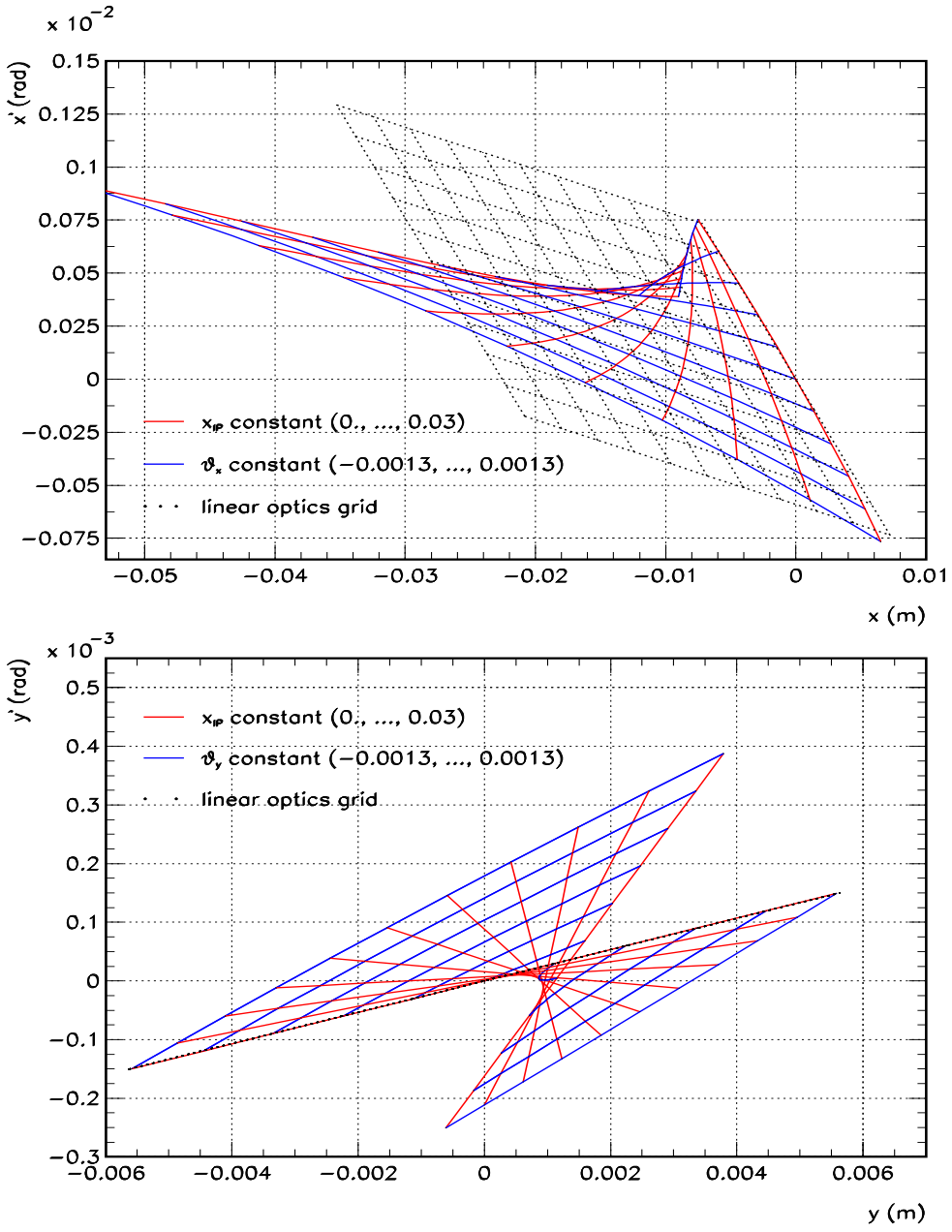

Figure 3: Iso-lines of constant emission angles θ_x, θ_y and fractional proton energy loss $x_{I\!P}$ in the planes defined by the quantities x, x', y, y' measured in the pots. The coordinates x and y are taken half way between the two pots. The full, coloured lines show the correlations with the angles of scattered protons for particles emitted at fixed θ_x, θ_y and $x_{I\!P}$ according to the new beam transport calculations. The dotted grid shows the same correlations for the linear beam optics.

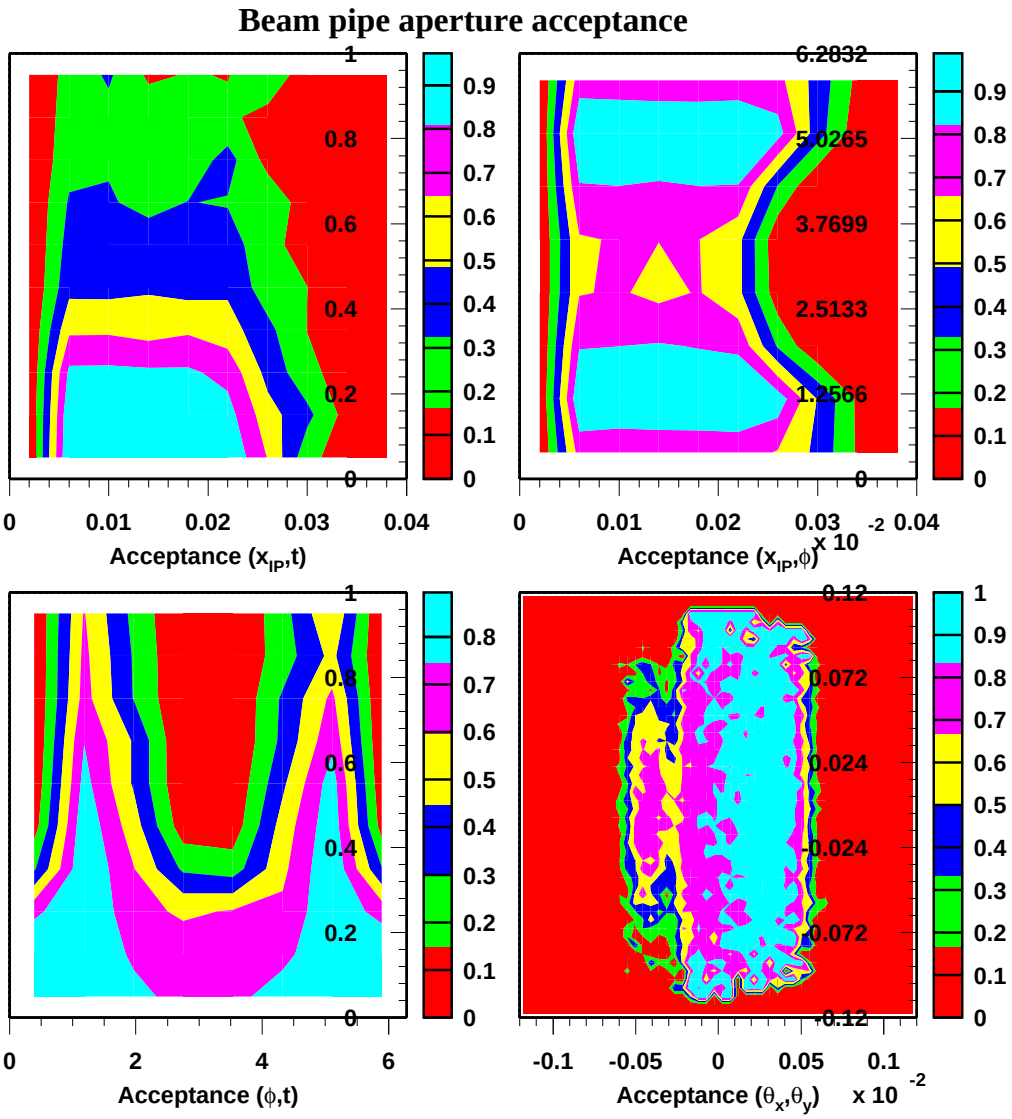

Figure 4: The VFPS acceptance as defined by the aperture of the beam pipe as a function of the pairs of variables ($x_{I\!P}$, t), ($x_{I\!P}$, ϕ), (ϕ, t) and (θ_x, θ_y). Values of t are given in GeV^2. All angles are in radians.

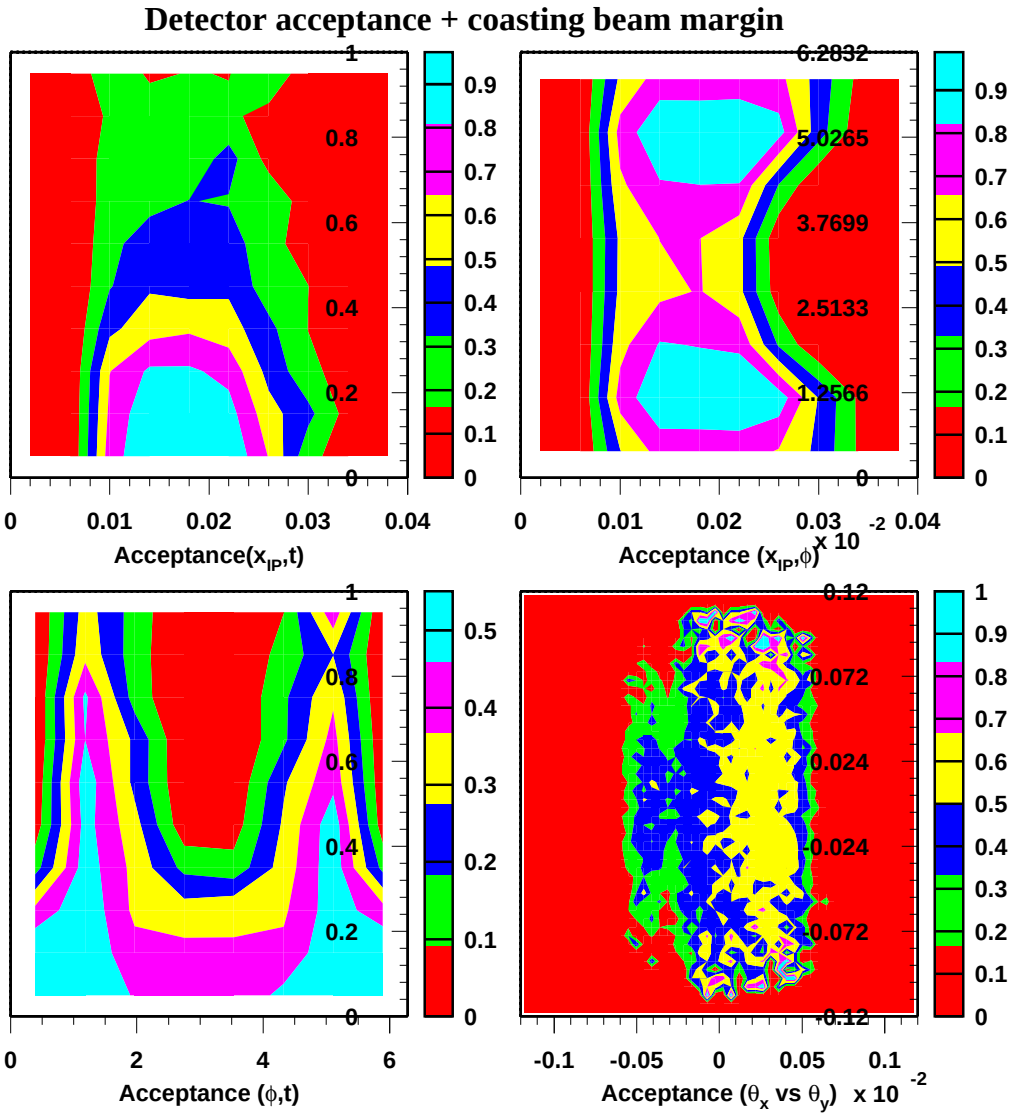

Figure 5: The VFPS acceptance when the detector is retracted by 3 mm to allow for a large coasting beam component as a function of ($x_{I\!P}$, t), ($x_{I\!P}$, ϕ), (ϕ, t) and (θ_x,θ_y). Values of t are given in GeV^2. All angles are in radians.

3 VFPS Resolutions and Calibration

3.1 Resolutions in $x_{I\!P}$, t and ϕ

As noted in section 2, the variables $x_{I\!P}$, t and ϕ are reconstructed using a χ^2 minimization procedure in which initial values for the parameters $x_{I\!P}$, θ_x and θ_y are required. Here we estimate the resolutions obtained on $x_{I\!P}$, t and ϕ using simulations based on the non-linear beam-optics and the minimisation procedure as discussed in section 2.

To obtain starting values of $x_{I\!P}$ for the minimisation procedure, we use the redundancy offered by the independent measurement of the photon dissociation system X in the central components of H1. This gives a measurement of $x_{I\!P}$ with a typical resolution $\Delta x_{I\!P}^{H1} \approx 0.005$. In the simulations, we therefore assume a starting value for $x_{I\!P}$ equal to the true value smeared according to this resolution. For the scattering angles θ_x and θ_y, a starting value of zero is assumed as no direct measurement from the central H1 detector is available.

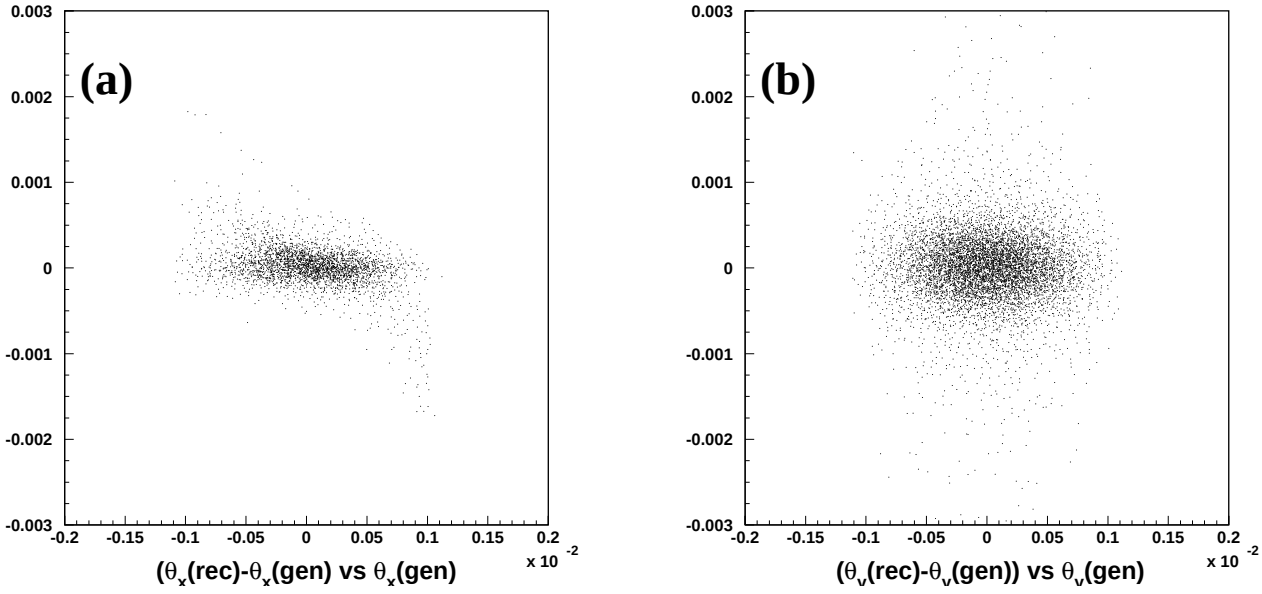

Figure 6: (a) Shifts $\theta_x\ (\mathrm{rec}) - \theta_x\ (\mathrm{gen})$ between the true and reconstructed value of θ_x plotted against the true $\theta_x\ (\mathrm{gen})$ from the simulated sample of events. (b) Shifts $\theta_y\ (\mathrm{rec}) - \theta_y\ (\mathrm{gen})$ between the true and reconstructed value of θ_y plotted against the true $\theta_y\ (\mathrm{gen})$.

Figures 6a and 6b show the shifts between the generated and reconstructed values of θ_x and θ_y respectively. The proximity of the lines of constant θ_x with the non-linear optics (see fig. 3a) leads to broad χ^2 minima and hence to a poorer resolution on θ_x than was originally hoped. This effect is completely determined by the beam optics and therefore represents an intrinsic limitation of the apparatus. If the chosen starting values are too far from the true values, there is also a finite probability of the minimisation procedure finding a false χ^2 minimum, resulting in further deterioration of the resolutions. This effect is strongest at large values of $|\theta_x(gen)|$, where the true value is furthest from the starting value of $\theta_x = 0$ (see fig. 6a). The deterioration

in resolution induced by these wrong solutions is dependent on the choice of reconstruction procedure and it is thus expected that the situation can be improved with more sophisticated algorithms. The non-linear beam optics have a less pronounced effect on the θ_y reconstruction, which is shown in fig. 6b.

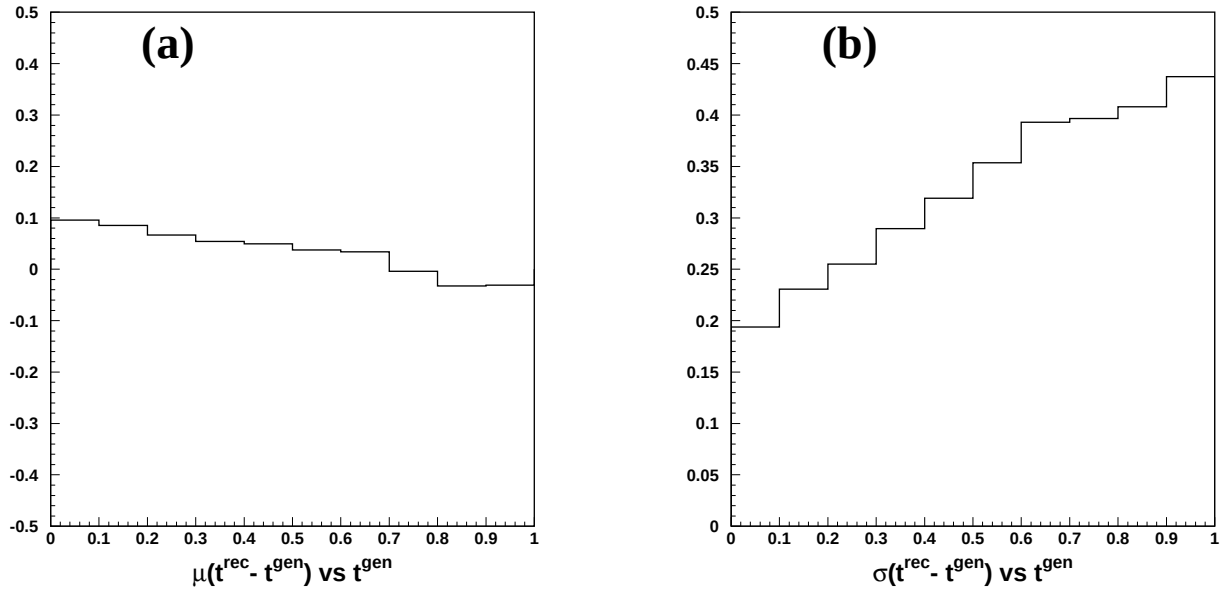

Figure 7: (a) Bias in t (mean shift of the reconstructed $t^{\rm rec}$ from the generated $t^{\rm gen}$) as a function of $|t^{gen}|$. (b) Resolution on t (Root mean squared width of the $t^{\rm rec} - t^{\rm gen}$) distribution as a function of $|t^{\rm gen}|$. All values are in GeV^2.

The quality of the t-reconstruction is shown in fig. 7. The bias in the θ_x(rec) and θ_y(rec) reconstructions results in a slight tendency to over-reconstruct $p_{\rm T}$ and hence gives rise to a positive bias in $|t|$, especially at low values (fig. 7a).

The resolution on t (fig. 7b) is approximately twice that obtained with the linear optics in the original proposal [1]. To investigate whether an improved spatial resolution of the detectors might help, we have repeated the procedure with the resolution set to $1\mu m$ in place of the expected $100\mu m$. The resulting resolutions are shown in fig. 8. The improvement in the t resolution is small, indicating that the resolution is principally determined by the proximity of the lines of constant θ_x in fig. 3.

The simulated bias and resolution for $x_{I\!P}$ from the assumed reconstruction procedure (using $\Delta x_{I\!P}^{H1} = 0.005$) are shown in fig. 9. Fig. 9a shows that the mean deviation between the reconstructed and the true values of $x_{I\!P}$ varies between 0.00075 and -0.0015. Fig. 9b indicates that the resolution on $x_{I\!P}$ roughly scales with $x_{I\!P}$ and is approximately constant at 10%. The first estimates of the $x_{I\!P}$ resolution in [1] gave an approximately constant value of 0.00075, corresponding to $\sim 8\%$ at $x_{I\!P} = 0.01$ and $\sim 2\%$ at $x_{I\!P} = 0.04$. The non-linear optics and the minimisation procedure thus lead to a slightly poorer resolution at the lowest $x_{I\!P}$ with larger effects at higher $x_{I\!P}$.

The bias and resolution of the reconstruction of the ϕ variable are shown as a function of ϕ and $|t|$ in fig. 10. The resolution on ϕ is comparable to the value in the proposal [1]. The bias is

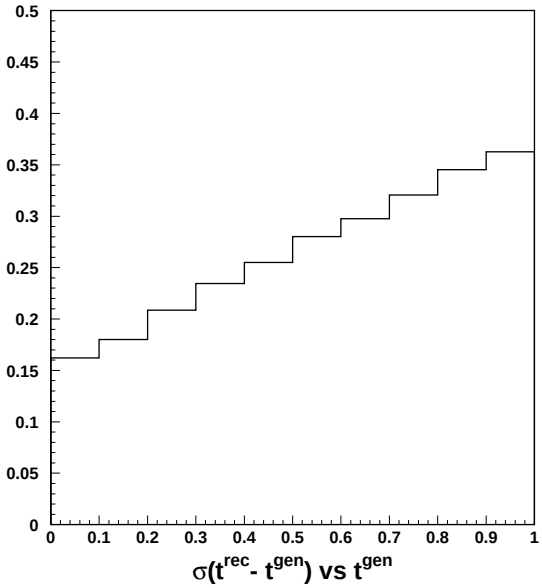

Figure 8: Resolution on t (Root mean squared width of the $t^{\rm rec} - t^{\rm gen}$) distribution as a function of $|t^{\rm gen}|$, assuming a 1 μm detector resolution. All values are in GeV^2.

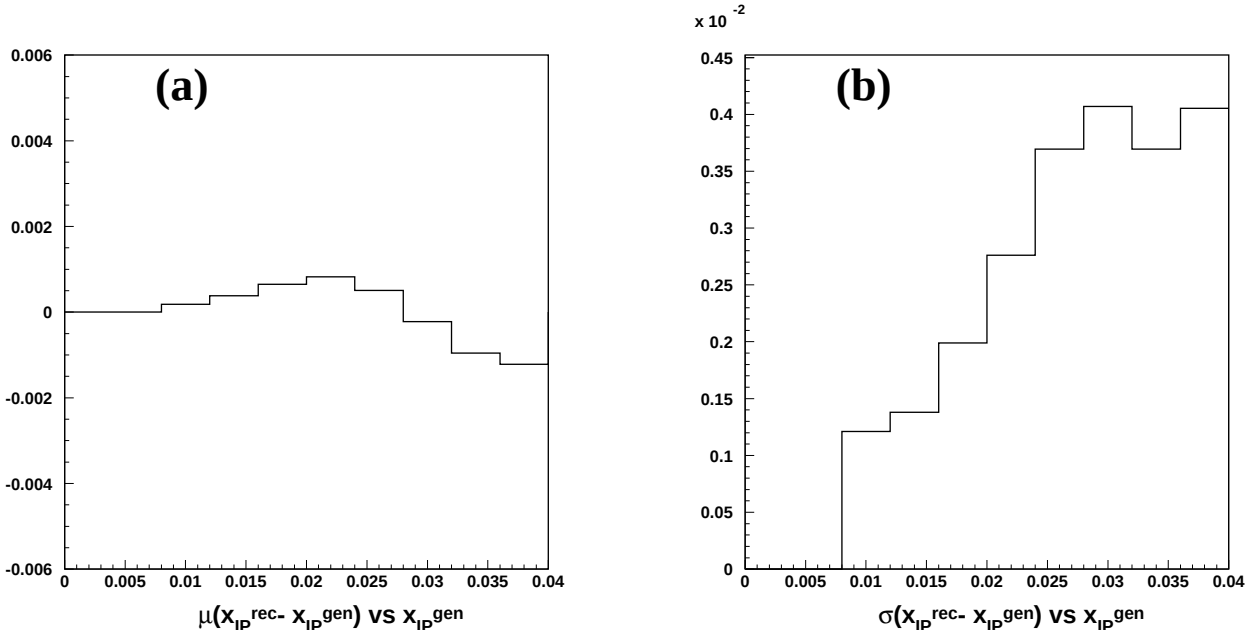

Figure 9: (a) Bias in $x_{I\!P}$ (mean shift of the reconstructed $x_{I\!P}^{\rm rec}$ from the generated $x_{I\!P}^{\rm gen}$) as a function of $x_{I\!P}^{\rm gen}$. (b) Resolution on $x_{I\!P}$ (Root mean squared width of the $x_{I\!P}^{\rm rec} - x_{I\!P}^{\rm gen}$) distribution as a function of $x_{I\!P}^{\rm gen}$.

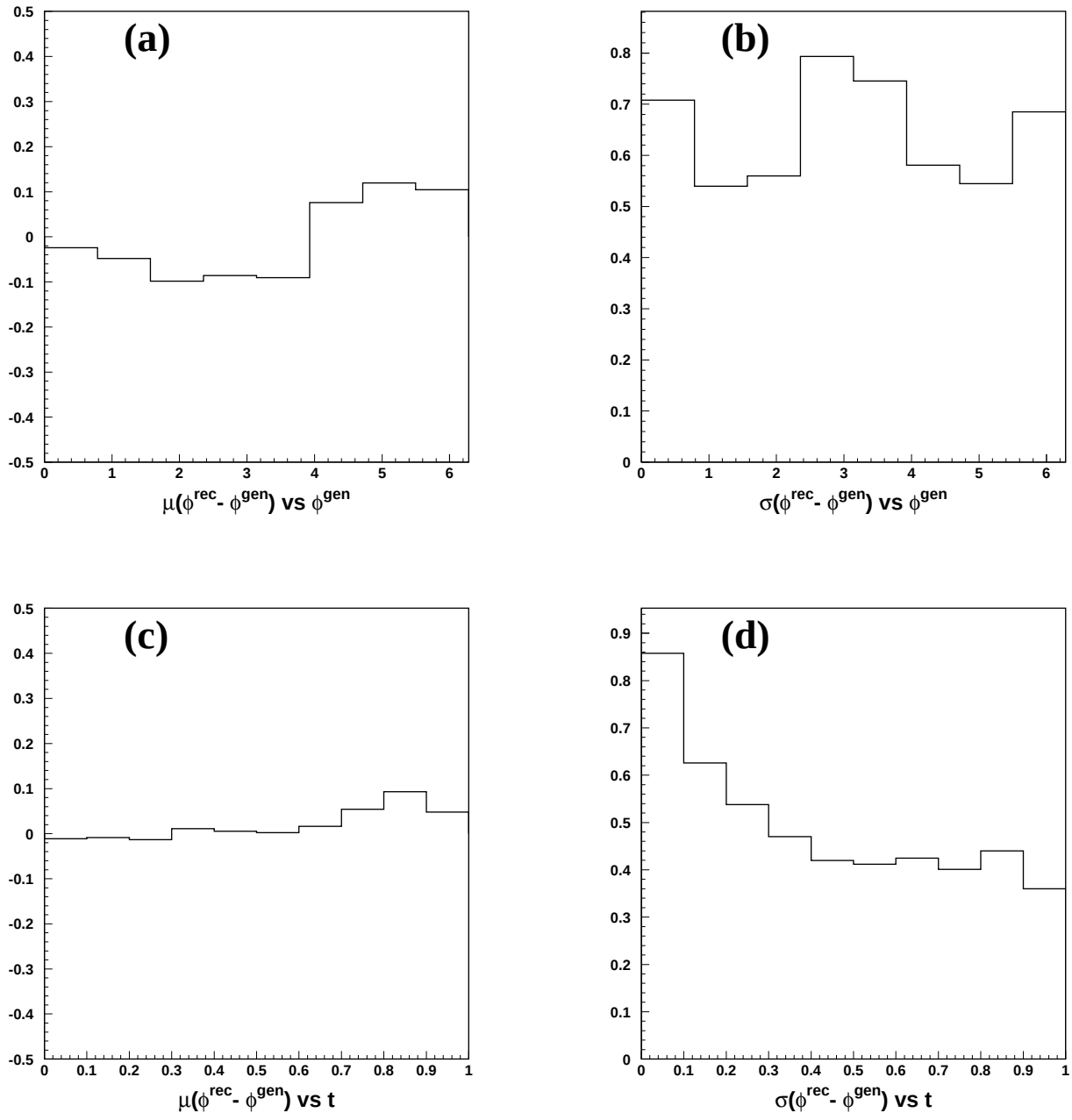

Figure 10: (a) Bias in ϕ (mean shift of the reconstructed $\phi^{\rm rec}$ from the generated $\phi^{\rm gen}$) as a function of $\phi^{\rm gen}$. (b) Resolution on ϕ (Root mean squared width of the $\phi^{\rm rec} - \phi^{\rm gen}$ distribution) as a function of $\phi^{\rm gen}$. (c) Bias in ϕ as a function of $|t|^{\rm gen}$. (d) Resolution on ϕ as a function of $|t|^{\rm gen}$. All ϕ values are in radians and all t values are in GeV^2.

small in comparison with the resolution. The resolution on ϕ also depends on t as can be seen in fig. 10d. At $|t| \to 0$, p_{T} and hence θ_x and θ_y also tend to zero, such that ϕ reconstruction becomes increasingly difficult.

The effect on the reconstruction of the variables $x_{I\!P}$, t and ϕ of different assumptions regarding the resolution on $x_{I\!P}$ from the central detectors has been investigated by assuming various values for $\Delta x_{I\!P}^{H1}$. For the unrealistically large value of $\Delta x_{I\!P} = 0.01$, the VFPS resolution on $x_{I\!P}$ becomes worse by a factor of 2, while the resolutions in t and ϕ remain largely unaffected.

3.2 Calibration: Sensitivity to Detector Positioning

A full calibration scheme for the VFPS detector was given in the VFPS proposal [1] for the case of linear beam optics. We are working towards a similar calibration scheme for the new beam simulation, including the sextupoles, though the results are not yet available. Here, we show that the potential exists for determining possible detector offsets on the basis of overall distributions in θ_x and θ_y. Since the physical processes giving rise to protons in the VFPS are azimuthally symmetric, deviations of the mean θ_x and θ_y can be interpreted as being due to shifts in the detector positioning and can be used for calibration.

Fig. 11a,b show the effect on the simulated θ_x and θ_y distributions of a 100 μm vertical shift on one of the two Roman pots for a sample of approximately 8000 events. The mean value of the θ_x distribution remains very close to zero, whereas the mean of the θ_y distribution is shifted by approximately 180 μrad. Similarly, fig. 11c,d show the effect of a 200 μm horizontal shift in one of the pots. The θ_y distribution is barely affected, whilst the θ_x distribution is again shifted by around 180 μrad. We thus conclude that the spatial positions of the detectors can be calibrated to better that 100 μm in the vertical direction and 200 μm in the horizontal direction with rather modest statistics.

3.3 Unfolding the Slope Parameter in *t*

Extracting the slope parameter b from the reconstructed t-distribution requires an unfolding procedure taking account of the resolutions and shifts obtained from the beam transport calculation. Work on the optimisation of such procedures is ongoing. Here, we show simulated results using the iterative unfolding procedure described in [4].

For these simulations, we generate a sample of "data" events with a particular t distribution, following $e^{b_{true}t}$. The events are then passed through the beam transport simulation with resolutions as described in section 3.1. The reconstructed t spectrum is unfolded using correlation matrices between generated and reconstructed events determined using a second Monte Carlo simulation with a different input t distribution following $e^{b_{MC}t}$. In the unfolding procedure, the value of b_{MC} is changed at each iteration in order to improve the agreement with the "data". The procedure is stopped when the χ^2 change between successive iterations becomes small ($\lesssim$10 iterations).

This exercise has been performed for a variety of input slope parameters in the range $1 < b_{MC} < 8$ GeV^{-2} and $1 < b_{true} < 8$ GeV^{-2}. In each case, it was found that the real value of

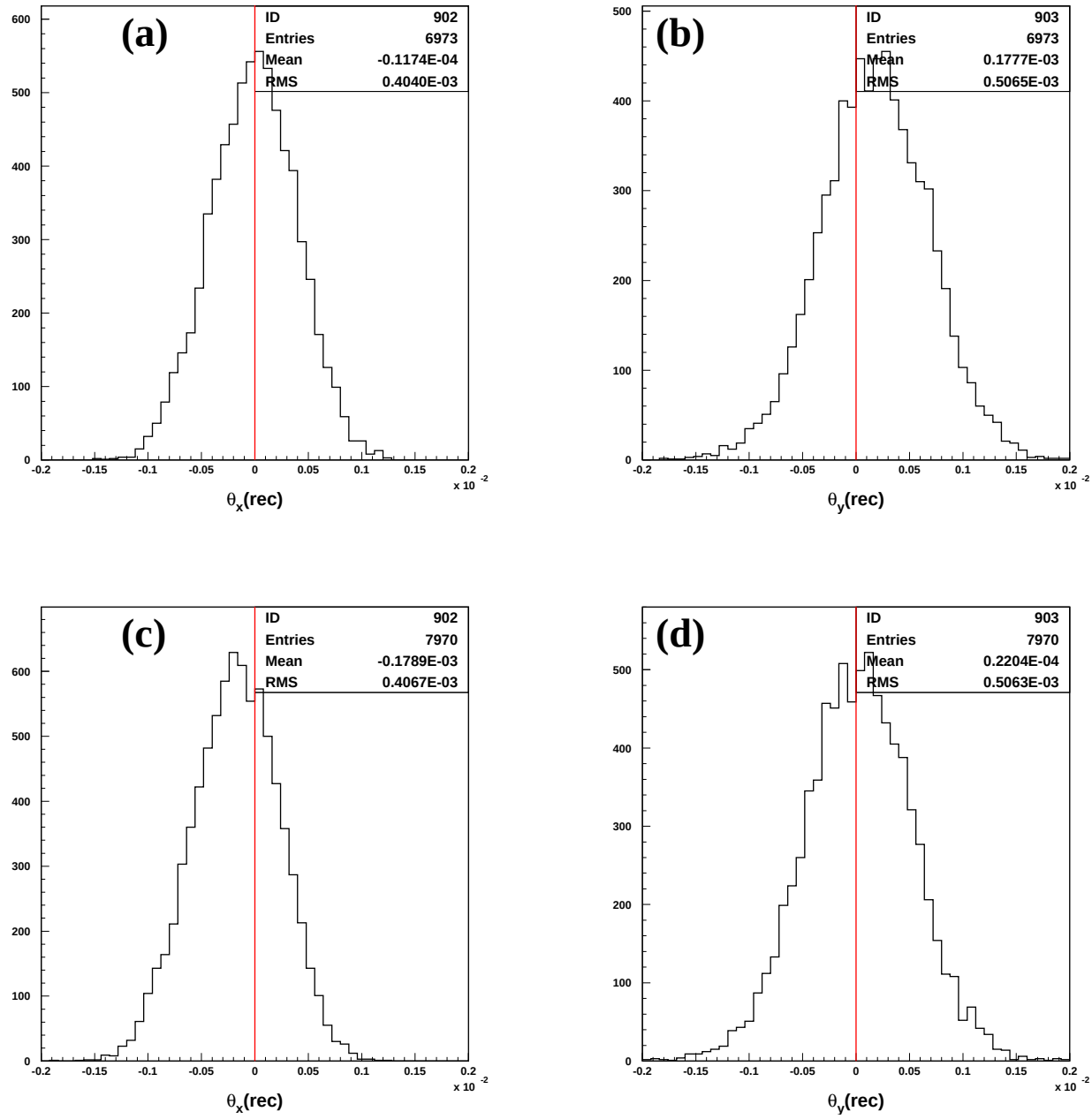

Figure 11: a),b) Reconstructed θ_x and θ_y distributions for a 100 μm vertical shift of one of the Roman pots; c),d) Reconstructed θ_x and θ_y distributions for a 200 μm horizontal shift of one of the Roman pots. All values of θ_x and θ_y are in radians.

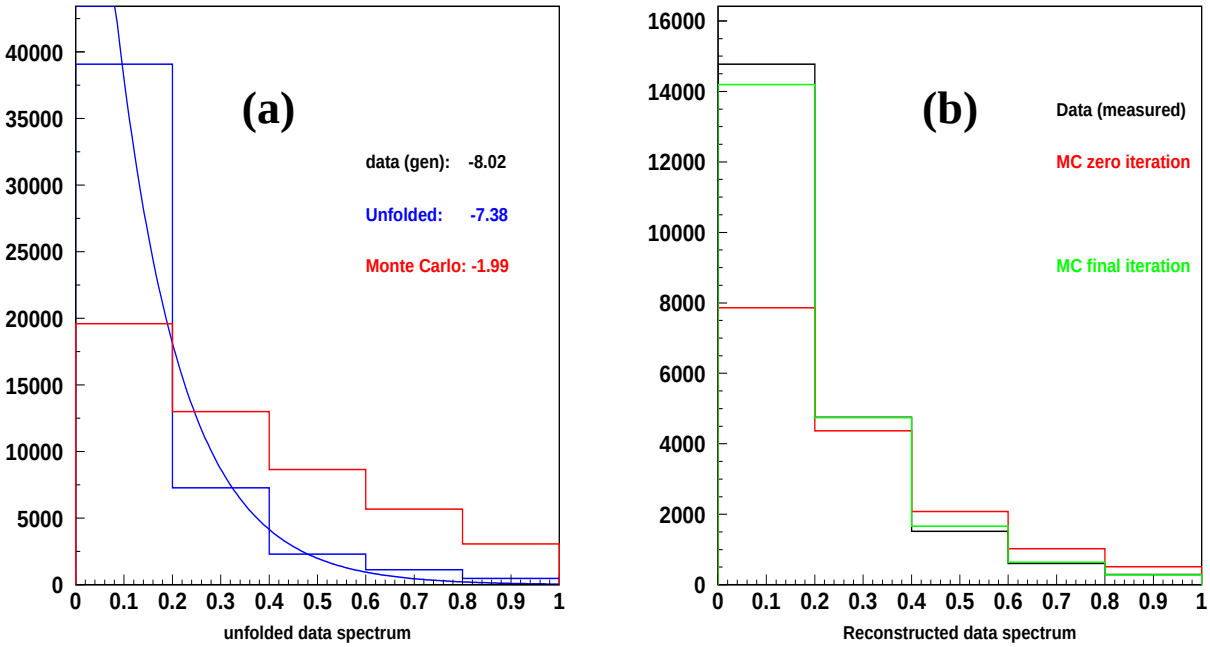

Figure 12: (a) Unfolded and (b) reconstructed t spectra obtained using a "data sample" with a b_{true} of 8 GeV^{-2}, unfolded using a Monte Carlo simulation with input b_{MC} of 2 GeV^{-2}. The "data" are shown in black, the starting Monte Carlo distribution in red and the result of the last iteration in green.

b_{true} in the data is determined to better than 1 GeV^{-2}. An extreme example is shown in fig. 12, where a "data" t-distribution with $b_{true} = 8$ GeV^{-2} is unfolded using a Monte Carlo simulation with $b_{MC} = 2$ GeV^{-2}. The unfolded value of b is within 1 GeV^{2} of b_{true}.

It is clear from these studies that the beam transport and finite spatial resolutions of the detectors do not completely obscure the information on t values in the data. It should be noted that calibration of the t spectrum will be possible using exclusive processes (e.g. vector meson production with decays to two charged tracks) where t is accurately reconstructed in the central detectors. Performing the unfolding of the VFPS t measurements on vector meson samples will allow us to identify possible problems in the procedure and estimate the inherent uncertainties.

The precision with which the b parameter can be extracted is dependent on the accuracy with which the correlation matrices used in the unfolding are known. The accuracy of these correlation matrices is determined by how well we are able to describe the beam line. Since the locations and fields of the beam magnets are in principle known rather precisely, we do not expect large systematic effects from this source. However, it is presently unclear which are the key parameters that influence the b slope extraction.

We have considered other potential sources of systematic error on the b slope. The effect of miscalibrations of the positions of one of the detectors by 100 μm in the vertical direction or 200 μm in the horizontal direction was shown to be visible using the measured data in section 3.2. Conservatively estimating this to be the precision with which the spatial positions of the detectors are known, we have simulated the effect on the b slope extraction of a systematic

shift by $180\ \mu\mathrm{rad}$ in either θ_x or θ_y. The result is a systematic uncertainty on the extracted b slope of $1\ \mathrm{GeV}^2$.

On the basis of recent measurements using the FPS [5], the remaining systematics are expected to be dominated by background processes entering the VFPS sample.[2] Random coincidences between background tracks in the VFPS and ep induced events with electrons in the SPACAL were estimated to contribute a background of $6 \pm 2\%$ to the FPS sample. Assuming this background is a factor of 6 larger for the VFPS (see section 4.2), that the size of the background can also be determined with a 30% error and taking the extreme case of a flat distribution in t, we estimate that the resulting systematic uncertainty on b is approximately $0.8\ \mathrm{GeV}^{-2}$. Proton dissociation processes were estimated to contribute approximately 3% to the FPS sample at $x_{I\!P} = 0.04$, becoming negligible in the lower $x_{I\!P}$ region of the VFPS acceptance. For a true slope parameter of $b_{true} = 6.5\ \mathrm{GeV}^{-2}$, we estimate that the systematic effect on the extracted b slope of adding a 3% background from proton dissociation with a reconstructed t distribution of $e^{2.5t}$ is to shift the measured b by $0.2\ \mathrm{GeV}^{-2}$.

Taking the unfolding uncertainty on b to be $1\ \mathrm{GeV}^{-2}$ and adding further uncertainties due to θ_x and θ_y miscalibration and background processes, we reach a crude, and probably conservative, estimate that the slope parameter can be determined with a systematic uncertainty of $2\ \mathrm{GeV}^{-2}$.

4 VFPS Trigger Potential

4.1 Triggering Diffraction in H1

After the upgrade, an increase by a factor of 5 in luminosity yields a total ep interaction rate in excess of $1\ \mathrm{kHz}$. Background rates may also increase. With such high rates, most of the H1 trigger bandwidth will be taken up with rare processes involving high transverse momentum final states. However, many processes of particular interest in HERA physics do not display such signatures. By upgrading the calorimeter [6] and tracking [7] triggers, it will be possible to collect large samples of processes involving heavy quarks or containing relatively low p_{T} jet topologies. However, these upgrades will not allow us to trigger the bulk of diffractive interactions.

The strategy for triggering diffractive DIS at HERA I was to use all events triggered on the basis of electromagnetic backward calorimeter (SPACAL) activity at relatively low threshold (e.g. $6\ \mathrm{GeV}$), combined with a minimal vertex requirement (from the MWPCs). Diffractive selections were applied only off-line. This strategy will no longer be viable after the upgrade, since SPACAL triggers will be heavily prescaled unless they occur in combination with a further trigger indicating a hadronic final state of particular interest. A strong track requirement would cut heavily into the acceptance for inclusive diffraction. New methods are thus needed if we

[2] The FPS measurements also have a sizeable systematic uncertainty arising from the track reconstruction efficiency, which is due to the relatively poor single hit efficiency. It is expected that the single hit efficiencies (and hence their uncertainties) will be improved considerably by replacing the photomultipliers. This uncertainty affects only the normalisation and thus has no effect on the b slope extraction.

are to reliably trigger on diffraction with $Q^2 \lesssim 100\ \mathrm{GeV}^2$ at HERA II. For $Q^2 \gtrsim 100\ \mathrm{GeV}^2$, the electron is scattered into the liquid argon calorimeter, where no prescaling is expected to be necessary.

H1 has considered triggering diffractive final states on the basis of rapidity gaps, thus pushing the main pre-upgrade method for off-line diffractive analysis to the trigger level. One possibility is to require an absence of activity in the most forward part of the liquid argon calorimeter. The forward muon trigger (FMT) has also been reconfigured, such that the region $3^\circ \lesssim \theta \lesssim 7^\circ$ is used as a diffractive veto trigger.[3] Although triggers based on an absence of forward detector activity are able to reduce rates considerably in combination with the SPACAL trigger, the rejection factors (FMT only) are around a factor of 3 for photoproduction background and more like a factor of 2 for beam-gas interactions [8]. Larger factors are required in order to trigger all diffractive SPACAL data. A further problem with gap-based triggers is that they are highly sensitive to changes in background and noise conditions, making precise efficiency calculations problematic.

It is thus clear that the only method of triggering diffraction after the upgrade that will meet the requirement of a large and well known efficiency in a specified kinematic range will be to use Roman Pot signals in the trigger. It has been shown that it is possible to provide trigger information based on a coincidence of signals in the two VFPS stations to the first level trigger of H1, with approximately 100 ns to spare within the required decision time. One of the main contributions of the VFPS will thus be to provide a highly efficient trigger for diffraction within its acceptance region.

In the next section, estimates are made of the rate at which a trigger based on a coincidence of a SPACAL electron with a minimal central vertex requirement (MWPCs) and a VFPS trigger would run.

4.2 Estimated Peak Rates for SPACAL Electrons

The rates estimated below are for the *maximum* post-upgrade luminosity. For average luminosities, the rates should be roughly halved. They are based on a luminosity increase to $70\ \mu\mathrm{b}^{-1}\mathrm{s}^{-1}$ and increases in the proton and electron beam currents by factors of approximately 2 to $160\ \mathrm{mA}$ and $58\ \mathrm{mA}$ respectively.

Background in the SPACAL calorimeter correlated with a vertex in the interaction region arises from photoproduction and beam-gas interactions in which a high energy hadron fakes the electron trigger. Background in the VFPS is expected to be entirely correlated with the proton beam.

Prior to the upgrade, the maximum rate for the combination of a SPACAL electron at $Q^2 \gtrsim 5\ \mathrm{GeV}^2$ and a minimal vertex trigger was approximately 100 Hz [7] and for a high energy electron (above 15 GeV) about 30 Hz. The inner part of the SPACAL, roughly corresponding to $\theta > 174^\circ$, has now been removed. This restricts the acceptance in a manner dependent on y, but corresponding approximately to $Q^2 > 8\ \mathrm{GeV}^2$.

[3] It is not possible to use more of the Forward Muon system for this veto without seriously compromising the efficiency for muon triggering

From the L2-L4 transparent run studied in [7], it is estimated that 30% of the rate in the SPACAL comes from $\theta < 174^\circ$. There has also been an upgrade to the proportional chambers, which may decrease the rate (e.g. by requiring a coincidence of more layers), though no account of this is taken in the calculations.

In order to be conservative, we assume that the rates from the combination of a SPACAL calorimeter and an MWPC vertex trigger scale with the luminosity rather than with the beam currents. We therefore estimate a maximum post-upgrade rate for this combination of 175 Hz.

In [3], Monte Carlo simulations suggested that the expected rate of coincident signals in the two stations of the VFPS is approximately a factor of 3 larger than that for coincidences in the two stations of the FPS. Prior to the upgrade, the FPS registered coincidence rates of up to 10 kHz. Assuming that this rate scales with the proton beam current, we estimate a post-upgrade VFPS coincidence rate of 60 kHz.

Approximately 97% of beam interactions giving rise to background in the VFPS occur in the warm section of the beamline between H1 and the Roman pots [3], the remaining 3% arising from interactions further upstream. By contrast, the beam interactions giving rise to SPACAL / MWPC triggers occur in the H1 interaction region or further upstream. The correlation between SPACAL and VFPS background is made smaller still by the fact that the upstream beam-gas interactions yielding VFPS background will be dominated by minimum bias low p_{T} processes, where $> 97\%$ of the proton beam energy is carried away by the leading proton, whereas the SPACAL triggers from this source arise from the tiny fraction of beam-gas interactions producing sufficiently high p_{T} particles to fake an electron in the SPACAL. Here, we neglect any correlation between background rates in the SPACAL and in the VFPS.

Given that bunch crossings take place at 96 ns intervals, the rate of random coincidences between a VFPS and a SPACAL / MWPC chamber trigger is

$$\begin{aligned} \mathrm{Rate\ VFPS} \times \mathrm{SPACAL/MWPC} &= \frac{(\mathrm{Rate\ VFPS}) \cdot (\mathrm{Rate\ SPACAL/MWPC})}{\mathrm{Bunch\ Crossing\ Frequency}} \\ &\sim 1.0\,\mathrm{Hz} \end{aligned}$$

The rate at which diffractive DIS events that can be triggered by the combination of the VFPS, the SPACAL calorimeter and the central MWPCs occur at $70\mu\mathrm{b}^{-1}\mathrm{s}^{-1}$ is estimated from Monte Carlo simulations to be $\sim 0.4\,\mathrm{Hz}$, such that the overall peak rate is estimated to be around $1.4\,\mathrm{Hz}$. The rate estimates given here are probably accurate to no better than a factor of 3. However, it is clear that the VFPS will provide a crucial triggering tool at acceptable rates. With the Fast Track Trigger providing accurate tracking information to the second level trigger [7], an extra requirement of a track with $p_{\mathrm{T}} \gtrsim 100\,\mathrm{MeV}$ could be imposed as is currently done in off-line F_2^D analysis. With this additional criterion, rates of well below 1 Hz are assured.

4.3 Triggering Exclusive Processes

Similar arguments can be made for the triggering of hard scattering processes in diffractive DIS and in photoproduction ($Q^2 \to 0$). The most interesting channels here are dijet and charm production and elastic heavy vector meson (J/ψ, Υ) production. These processes are all integral

parts of the investigation of diffraction at HERA II. With the use of small angle electron taggers 6 m and 40 m downstream, the fast track trigger and the jet trigger, all of these channels can be triggered [6, 7] without a diffraction-specific trigger, though the trigger rates may be high, especially for dijet production at low p_{T}. It is clear that the additional use of the VFPS trigger will allow us to keep trigger conditions as loose as possible for these processes.

For light vector meson electroproduction and the DVCS processes (see section 5.7), a high energy (above 15 GeV) is always required in the electromagnetic SpaCal. The expected rate with this threshold, based on the measured rates in 1997 and 1999 and including the effect of the inner SpaCal removal, is about 30 Hz. These rates are not acceptable as such. Combining the high threshold SPACAL trigger with the VFPS trigger will reduce the rate to 0.2 Hz (again assuming a rate of 60kHz for the VFPS trigger, uncorrelated with the SPACAL rate). The number of DVCS events available for analysis with and without the VFPS trigger are given in section 5.7.

5 Physics Potential of the VFPS

5.1 Introduction

Some of the most interesting questions in diffractive DIS relate to its factorisation properties. In [9], collinear factorisation was proven for a general class of semi-inclusive processes in DIS, where the final state contains an identified particle with particular 4-momentum. Under these circumstances, it is possible to define associated parton densities for the proton, which should evolve with Q^2 according to the usual DGLAP equations. A particular case of semi-inclusive production is a leading proton with specified values of $x_{I\!P}$ and t, corresponding to the final states measured in diffractive DIS at HERA. This is the most promising channel in which to perform tests of the semi-inclusive factorisation theorem and thus of the predictions of QCD for diffraction.

The programme of measurements required to perform this factorisation test would begin by obtaining very high precision F_2^D data on the β and Q^2 dependence at a fixed value of $x_{I\!P}$, either at fixed t or integrated over a fixed t range. Collins proof [9] then allows us to extract diffractive parton densities at these $x_{I\!P}$ and t values through DGLAP fits in the relatively large Q^2 region where higher twist contributions (e.g. vector mesons) and possible saturation effects [10] can be neglected. The region of the SPACAL calorimeter available at HERA II, corresponding to $Q^2 \gtrsim 8\ \mathrm{GeV}^2$, is perfect for this exercise. High precision on the β and Q^2 dependence is crucial in order to extract the diffractive gluon density on the basis of scaling violations with relatively small uncertainties. Comparing predictions based on these diffractive parton densities with hadronic final state information in diffraction (e.g. jet and charm data) at identical values of $(x_{I\!P}, t)$ would represent a unique test of semi-inclusive factorisation.

A second factorisation hypothesis, often termed 'Regge factorisation' or the Ingelman-Schlein model, amounts to a statement that the diffractive parton densities extracted in diffractive DIS have no dependence on $x_{I\!P}$ or t and can be considered as representing the partonic structure of the diffractive exchange or pomeron. Regge factorisation has no firm basis in QCD,

but arises through the success of the idea of a universal pomeron exchange in soft hadronic physics [11]. No deviations from Regge factorisation have yet been observed within diffractive DIS [12], though the effective pomeron intercept describing the process is larger than that in soft hadronic physics, suggesting that there is no universal pomeron. It is very important to continue to test Regge factorisation, for example by searching for variations in the effective pomeron intercept $\alpha_{I\!P}(0)$ with β or Q^2 within diffractive DIS data or variations in diffractive parton densities with $x_{I\!P}$ or t.

In the following sections, the physics potential of the VFPS is addressed both for inclusive measurements and for exclusive final states. The expected performance of the VFPS is compared with measurements using rapidity gap methods, with the existing H1 FPS and the now decommissioned ZEUS LPS. All studies shown are based on an integrated luminosity of $350\ \mathrm{pb}^{-1}$ for which the VFPS will be operational. This assumes three years of operation, with approximately 50% of the full luminosity delivered available for analysis.

5.2 Rapidity Gap and Leading Proton Methods

Two methods have been used to identify and measure diffractive events of the type $ep \to eXp$ to date:

1. **Reconstruction of X:** Here, the event kinematics are determined by measurement of the hadrons comprising X in the central components of the detector. The scattered proton or its excitation leaves the interaction region unseen down the forward beampipe. Usually an absence of activity is required in the forward region of the main detectors and in further instrumentation sensitive to energy flow at large pseudorapidities (rapidity gap method).

2. **Leading Proton Measurements:** Here, the scattered proton is detected and measured in the forward proton spectrometers.

Method 1 has yielded the most precise data to date, since it has been possible to use data efficiently triggered as a subset of the inclusive low Q^2 DIS sample, in the backward electromagnetic calorimeter (SPACAL). Although the statistical precision achieved by this method is high, such measurements are now limited by systematics associated with the unseen outgoing proton. The efficiency for rejecting proton dissociation processes is not perfectly known, nor are the relative cross sections for the proton-elastic and proton-dissociation channels and the dissociation mass (M_{Y}) and t dependences. The resulting systematic errors are at the level of 10% [12].

Measurements of F_2^D by the rapidity gap method are already being used to test the factorisation properties discussed in section 5.1 [12], though it has not been possible to date to extract separate parton densities at different values of $x_{I\!P}$ and t. Even when Regge factorisation is assumed when performing DGLAP fits to the present data, the limited statistics at high Q^2, the large systematics associated with the rapidity gap selection and the problems associated with the separate $x_{I\!P}$ dependences of the pomeron and sub-leading exchange contributions imply that the gluon density will still be measured to no better than 30% at low Q^2 with the present data.

To date, method 2 has suffered from statistical limitations, due to the relatively poor acceptances (a few %) of the leading proton spectrometers. Both H1 and ZEUS released Roman pot data with much improved precision at the recent EPS-2001 conference [5, 13]. However, even taking the full data available from HERA I, only a few thousand events are available for analysis. Despite the statistical limitations encountered up to now, the proton tagging method does not suffer from the large systematic uncertainties associated with the proton dissociation channel. Measurements can be made for unambiguous elastic-proton final states, over well defined ranges of t, or even at fixed t. With sufficient statistics, proton tagging should become the method that will yield the best precision on diffractive measurements.

5.3 Complementarity of FPS and VFPS

The existing H1 horizontal Roman pots (FPS) and the VFPS will provide complementary information which, if used in combination, will cover most aspects of diffractive electron-proton scattering. The horizontal FPS covers the range $0.08 < |t| < 0.45\ \mathrm{GeV}^2$ over a wide range in $x_{I\!P}$, albeit with an acceptance of only a few per cent. (see e.g. fig. 2 of [1]). The $x_{I\!P}$ coverage extends from the kinematic limit ($x_{I\!P} = x$) to $x_{I\!P} \sim 0.09$. Preliminary FPS results using all available pre-upgrade data ($29\ \mathrm{pb}^{-1}$) can be found in [5]. The total sample size was approximately 3000 events, but a 3-fold differential measurement in β, Q^2 and $x_{I\!P}$ and measurements of the t-slope parameter in 4 bins of $x_{I\!P}$ were already possible. With the full HERA II dataset, a sample size in the region of 50-100k events is expected, from which it will be possible to make precise measurements of the $x_{I\!P}$ dependence (and hence $\alpha_{I\!P}(0)$) and to search for variations in the t dependence with $x_{I\!P}$ (the α' / shrinkage question). However, these statistics will not permit the high precision extraction of diffractive parton densities at fixed $x_{I\!P}$ and t.

By contrast, the VFPS covers a limited range in $x_{I\!P}$ (see section 2) but has a very high acceptance in the region covered ($\sim\ 100\%$ for $|t| \lesssim 0.25\ \mathrm{GeV}^2$, falling to around 25% for $|t| = 0.8\ \mathrm{GeV}^2$). Thus, the VFPS is not optimised for measurements of the effective pomeron trajectory, but is expected to yield data with high statistical precision in a restricted region of $x_{I\!P}$, from which detailed tests of diffractive hard scattering factorisation will be possible.

The existing vertical FPS consists of Roman pots at 81 m and 90 m, which cover a higher $x_{I\!P}$ region than the horizontal FPS or the VFPS, with an acceptance of $\approx 20\%$ (see e.g. fig. 2 of [1]). Combining data from all three sets of pots will thus yield high statistics throughout a large kinematic region in $x_{I\!P}$ and t.

5.4 Inclusive Diffraction and Factorisation Tests with the VFPS

In this section, a feasibility study is presented for measurements of the β and Q^2 dependence of the diffractive structure function F_2^D, from which diffractive parton densities could be obtained and tested using final state dijet and charm data.

The ability of the VFPS to efficiently trigger the data over a restricted range of $x_{I\!P}$ and t (see section 4) implies that the dijet and charm data can be collected as part of the same sample as the inclusive data. These identical trigger conditions will considerably reduce the systematics

on the comparisons compared to the present data, where dijet and charm data are collected using triggers with harsher track conditions than is the case for the inclusive data. Furthermore, the dominant systematics on the VFPS measurements depend to first order on $x_{I\!P}$ and t only.[4] Since systematic errors associated with the proton measurement in the VFPS are not expected to vary significantly with x and Q^2 as extracted from the central detector, they appear as normalisation uncertainties in measurements of the β and Q^2 dependence in fixed regions of $x_{I\!P}$ and t. These systematics also cancel when making the comparisons of diffractive parton densities extracted from F_2^D with dijet or charm data also obtained with the VFPS. The systematic uncertainties which affect the measured kinematic distributions in β and Q^2 measurements in principle could be reduced to the 2-3% achieved in F_2 measurements [14]. For the present study, these errors are taken to be 5% in each bin, arising dominantly from the unfolding procedure in β and Q^2 and from detector calibration and energy scales.

The simulated measurements are shown for a single $x_{I\!P}$ bin centred on $x_{I\!P} = 0.017$ in order to maximise statistics throughout the phase space. It is assumed that all data from the VFPS will be used in the $x_{I\!P}$ region where the acceptance is large and approximately constant under the conditions where the coasting beam restricts the Roman pots to approximately 3.5 mm from the beam, namely $0.011 < x_{I\!P} < 0.024$. The t range is restricted to $|t| < 0.8$ GeV^2, where the acceptance remains reasonable. Acceptance effects are accounted for as described in section 2.

If the coasting beam turns out not to be a problem, then the high and constant acceptance region is extended to $0.004 < x_{I\!P} < 0.024$, which might allow a second $x_{I\!P}$ bin with similar statistics centred around $x_{I\!P} = 0.007$ covering the same region of t. Although this lower $x_{I\!P}$ range corresponds to the 'truly diffractive' region where in Regge models there is almost pure pomeron exchange, it is also the region where dijet and charm production are kinematically suppressed, so is less useful for testing extracted parton densities using hadronic final state data. From the point of view of the semi-inclusive factorisation tests that are under discussion here, the presence or absence of secondary exchanges is simply not an issue. It is the integrated diffractive parton densities to which collinear factorisation applies. Whether or not the coasting beam restricts the location of the VFPS, using data in a region where the VFPS has falling acceptance would allow measurements of only slightly lower quality in the region $0.024 < x_{I\!P} < 0.034$.

The simulated measurements are obtained using the RAPGAP [15] Monte Carlo model, used in an identical manner to that described in [12]. It is assumed that all diffractive data with electrons in the electromagnetic SPACAL ($\theta_e < 174^\circ$) and Liquid Argon calorimeters can be used. In order to ensure good kinematic reconstruction and suppress photoproduction background, a vertex from the central or forward tracker is required within 3σ of the nominal position. To reduce background from photoproduction processes, the electron energy is required to be greater than 8 GeV. Accepted events are required to satisfy $\eta_{\max} < 3.3$ to ensure that the system X is fully contained in the central detector, yielding a measurement of $x_{I\!P}$ independent of the VFPS. This redundancy proved very powerful in [5] to remove background from random coincidences in the VFPS and SPACAL and is therefore necessary to keep systematic errors to a minimum. It is also required to guarantee good $x_{I\!P}$ resolution from the VFPS (see section 3.1).

The total expected VFPS event yields are shown in table 1 for a variety of different conditions. Very high statistics are expected throughout most of the phase space, allowing high precision measurements in most channels. For the measurements of ϕ dependences (section 5.6)

[4] These systematics were discussed in section 3.3.

more than 10,000 events are expected in each of the 15 bins in the region where ϕ can be reliably reconstructed ($|t| \gtrsim 0.2\ \mathrm{GeV}^2$).

Sample	**No coasting beam**	**Coasting Beam**
All events	2,100,000	1,000,000
Acceptance $> 80\%$	1,100,000	390,000
Acceptance $> 80\%$, $I\!P$ only	930,000	280,000
$0 < \|t\| < 0.2\ \mathrm{GeV}^2$	1,800,000	810,000
$0.2 < \|t\| < 0.2\ \mathrm{GeV}^2$	330,000	160,000
$0.4 < \|t\| < 0.6\ \mathrm{GeV}^2$	47,000	23,000
$0.6 < \|t\| < 0.8\ \mathrm{GeV}^2$	6,000	3,000

Table 1: Expected VFPS yields for an integrated luminosity of $350\mathrm{pb}^{-1}$.

The data are binned in x and Q^2 using the same binning scheme as [14]. The differential cross section $\mathrm{d}\sigma/\mathrm{d}x\mathrm{d}Q^2\mathrm{d}x_{I\!P}(\mathrm{d}t)$ is then extracted, using the $x_{I\!P}$ measurement from the VFPS. This differential cross section is then converted to an $F_2^D[\beta, Q^2, x_{I\!P}, (t)]$ using $\beta = x/x_{I\!P}$.

The resulting simulated measurements for bins with high combined VFPS and central detector acceptance are shown in figures 13 and 14. It is clear that the statistical precision on the measurements remains high up to large Q^2. The kinematically accessible region in β and Q^2 for $x_{I\!P} = 0.017$ yields a large number of bins and is well suited to an extraction of the diffractive parton densities.

In section 3.3 the resolutions of the VFPS in t were shown. Using these resolutions as a guide, it is expected that measurements will be possible in 3 bins of t, corresponding to $0 < |t| < 0.2\ \mathrm{GeV}^2$, $0.2 < |t| < 0.45\ \mathrm{GeV}^2$ and $0.45 < |t| < 0.8\ \mathrm{GeV}^2$. It will be very interesting to search for variations in the β and Q^2 dependence or in the diffractive parton densities as a function of t. Since many QCD models of diffraction (e.g. [10, 16]) predict the diffractive cross section at $t = 0$ and insert the slope parameter b by hand, measurements in different t intervals are crucial for precise comparisons with models. The simulated measurements of $F_2^{D(4)}$ with this t binning scheme are shown in figures 15 - 17. The measurement becomes statistically limited only at the highest $|t|$ and the highest Q^2.

Unfortunately, it is not yet possible to estimate the precision expected on the extracted diffractive parton densities, since H1 is still in the process of developing methods to obtain errors on diffractive parton densities. However, it is clear from the quality of the expected measurement and the possibility of making measurements of the full β and Q^2 dependence at fixed $x_{I\!P}$ and t, that the prospects with the VFPS are far superior to any previous measurements or anything that will be possible by alternative methods at HERA II.

5.5 Hadronic Final States

As discussed in section 5.1 (see also [1]), diffractive charm and dijet production are particularly powerful tools for the understanding of the underlying dynamics, since they are directly sensitive to the role of gluons in the exchange. The VFPS offers the possibility of comparing

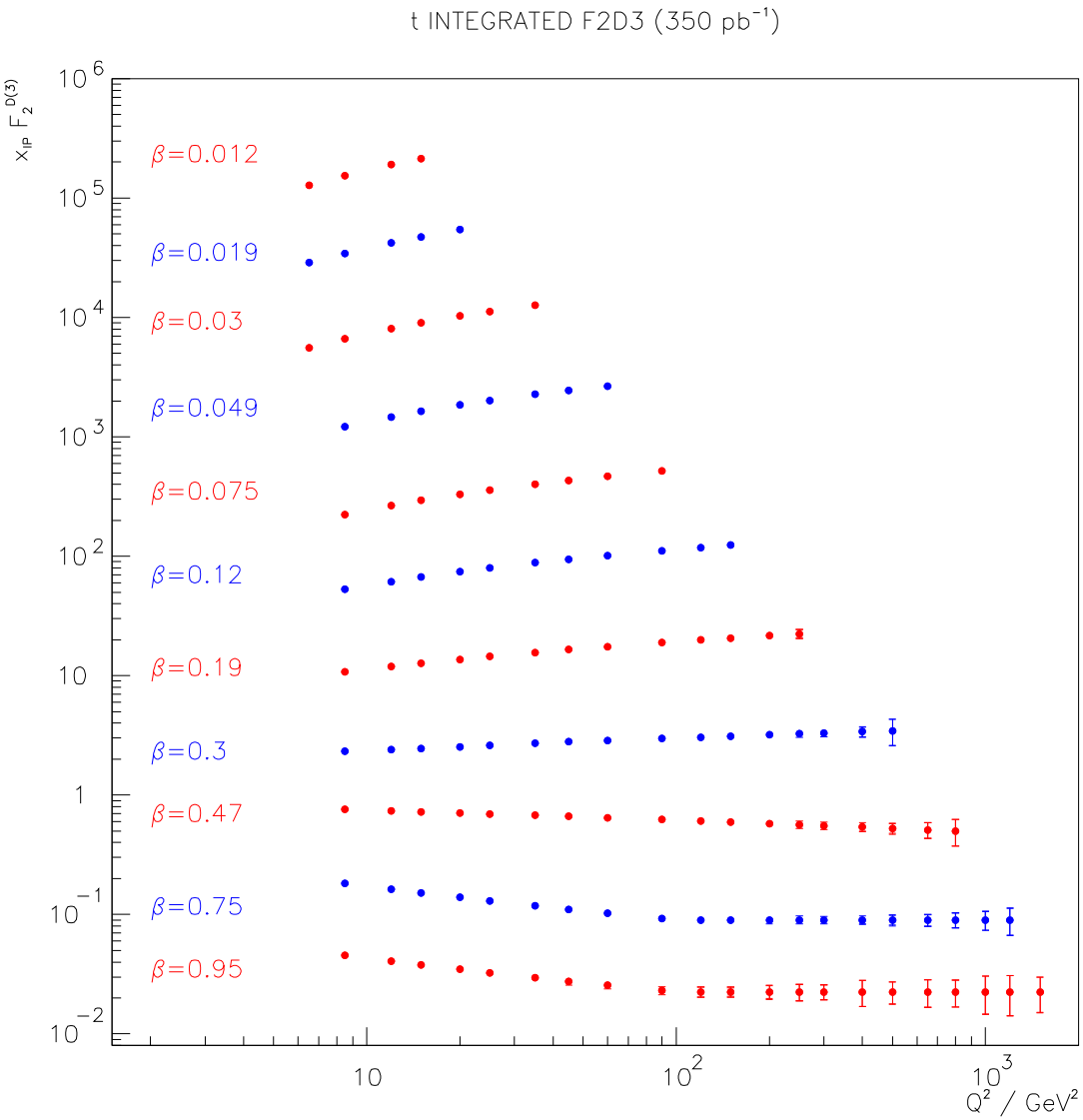

Figure 13: Expected precision for 350 pb^{-1} on $F_2^{D(3)}(\beta, Q^2, x_{I\!P})$ at $x_{I\!P} = 0.017$, integrated over $|t| < 0.8\ \mathrm{GeV}^2$, measured in the region $0.011 < x_{I\!P} < 0.024$, where the VFPS acceptance is large, even if the detector has to be ~ 3.5 mm from the beam due to the coasting beam. The data points at different β values are scaled by arbitrary factors for visibility.

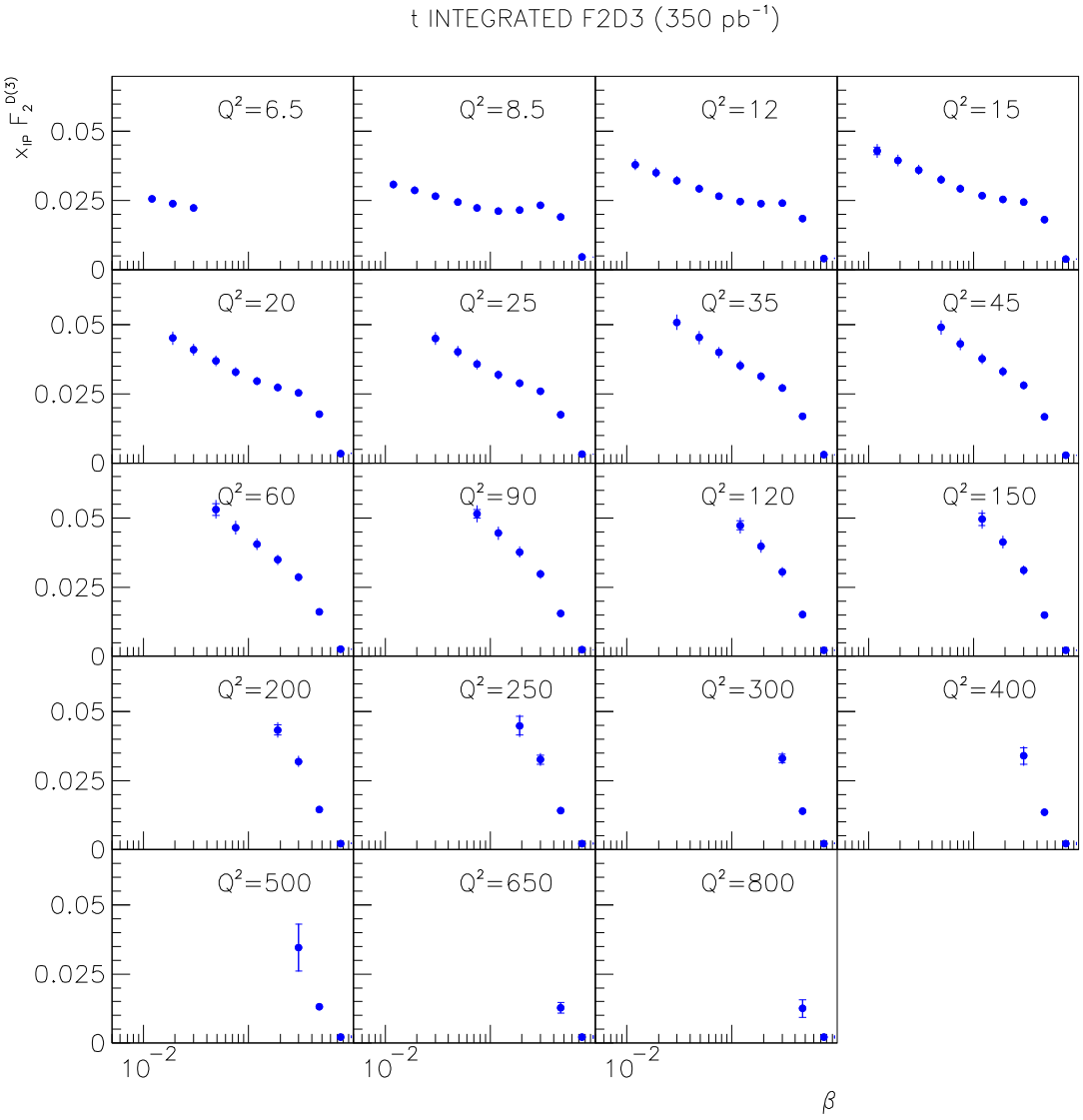

Figure 14: Expected precision for $350\ \mathrm{pb}^{-1}$ on $F_2^{D(3)}(\beta, Q^2, x_{I\!P})$ at $x_{I\!P} = 0.017$, integrated over $|t| < 0.8\ \mathrm{GeV}^2$, measured in the region $0.011 < x_{I\!P} < 0.024$, where the VFPS acceptance is large, even if the detector has to be $\sim 3.5\ \mathrm{mm}$ from the beam due to the coasting beam. The inner error bars show the expected statistical errors. The outer error bars show the statistical errors added in quadrature with the expected non-normalisation systematic errors. Further normalisation uncertainties arising from the VFPS (see text) are not shown.

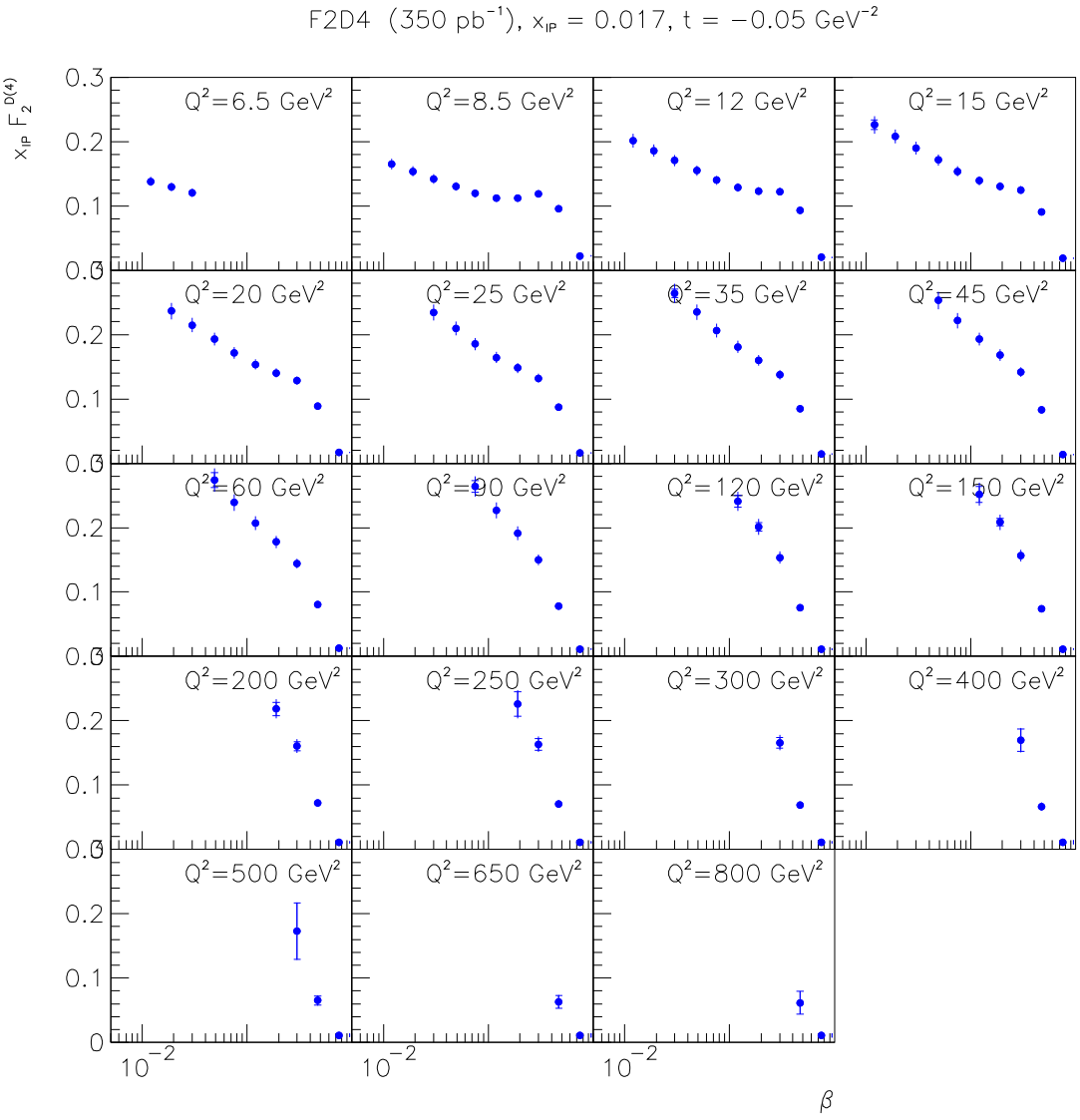

Figure 15: Expected precision for 350 pb^{-1} on $F_2^{D(4)}(\beta, Q^2, x_{I\!P}, t)$ at $x_{I\!P} = 0.017$ and $t = -0.05$ GeV^2, measured in the region $0.011 < x_{I\!P} < 0.024$ and $0 < |t| < 0.2$ GeV^2. The inner error bars show the expected statistical errors. The outer error bars show the statistical errors added in quadrature with the expected non-normalisation systematic errors. Further normalisation uncertainties arising from the VFPS (see text) are not shown.

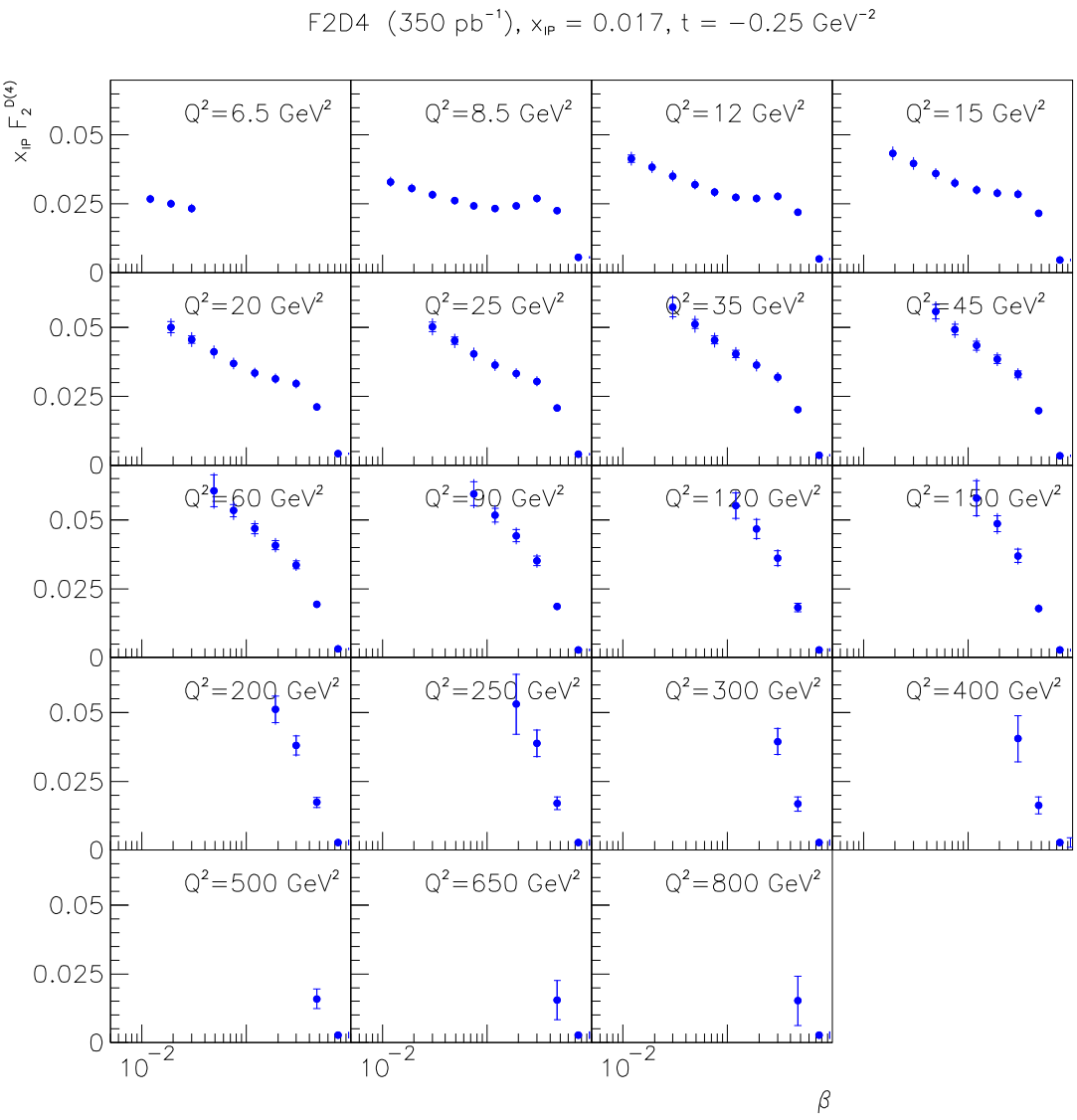

Figure 16: Expected precision for 350 pb^{-1} on $F_2^{D(4)}(\beta, Q^2, x_{I\!P}, t)$ at $x_{I\!P} = 0.017$ and $t = -0.25$ GeV^2, measured in the region $0.011 < x_{I\!P} < 0.024$ and $0.2 < |t| < 0.45$ GeV^2. The inner error bars show the expected statistical errors. The outer error bars show the statistical errors added in quadrature with the expected non-normalisation systematic errors. Further normalisation uncertainties arising from the VFPS (see text) are not shown.

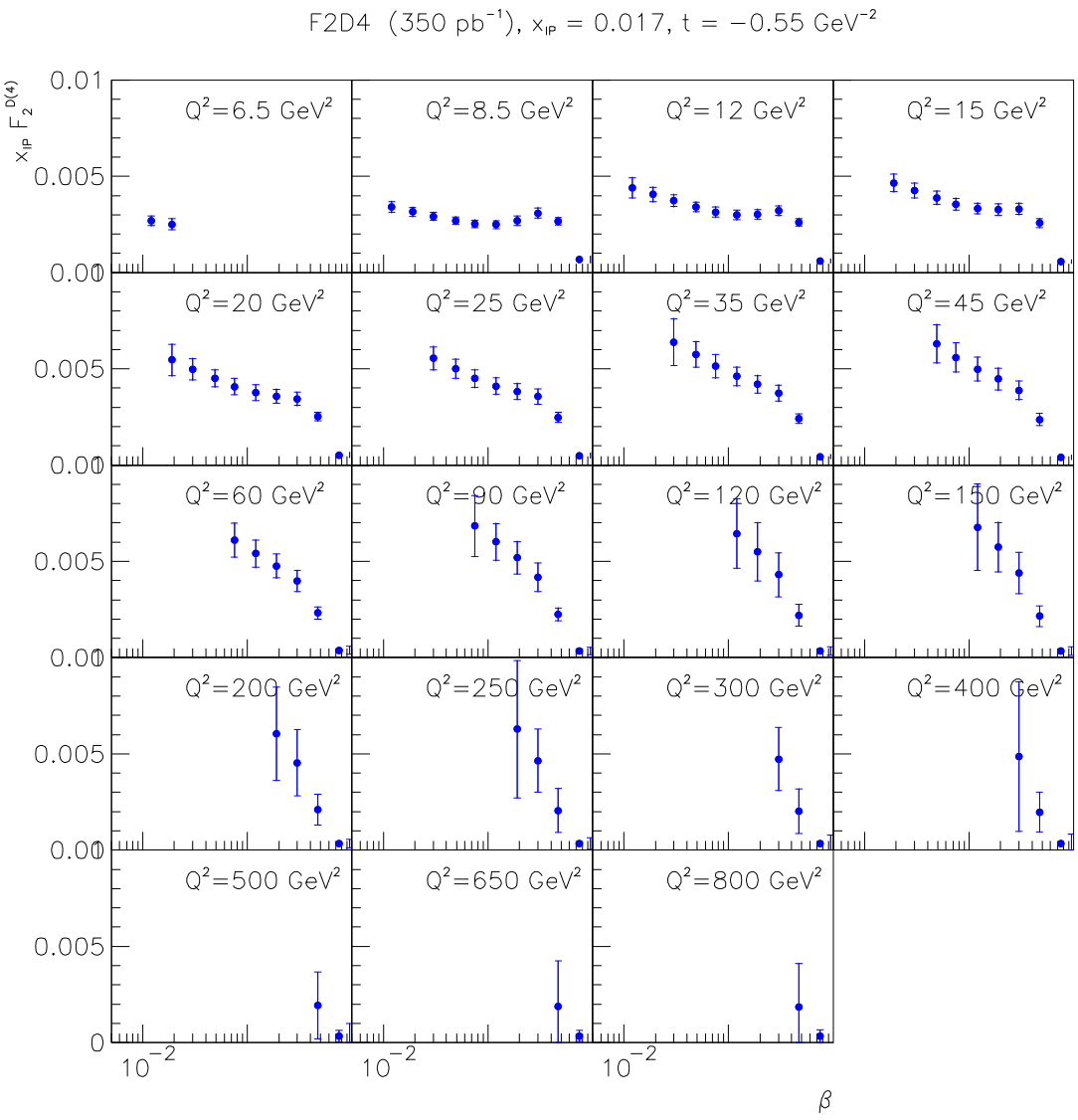

Figure 17: Expected precision for 350 pb^{-1} on $F_2^{D(4)}(\beta, Q^2, x_{I\!P}, t)$ at $x_{I\!P} = 0.017$ and $t = -0.55$ GeV^2, measured in the region $0.011 < x_{I\!P} < 0.024$ and $0.45 < |t| < 0.8$ GeV^2. The inner error bars show the expected statistical errors. The outer error bars show the statistical errors added in quadrature with the expected non-normalisation systematic errors. Further normalisation uncertainties arising from the VFPS (see text) are not shown.

measurements of these processes with predictions based on diffractive parton densities extracted from inclusive diffractive data using a common region of $x_{I\!P}$ and t with resulting cancellations of systematic effects. The statistics expected from the VFPS for these two channels are estimated below and are compared with the yields expected from pre-upgrade data.

5.5.1 Open Charm production

Cross sections for diffractive open charm production in DIS have been measured by H1 using the channel $D^* \rightarrow D^0\pi_{\rm slow} \rightarrow K\pi\pi_{\rm slow}$ [17]. The statistics available from the 1996 and 1997 data used in that analysis amounted to only 46 ± 10 events. The conclusions were correspondingly limited, though the measured cross sections were approximately 2σ smaller than predictions based on parton densities extracted from F_2^D. This is the only channel in diffraction at HERA where a suggestion of deviations from factorisation have been observed and it is therefore highly important to repeat the measurements with improved precision.

Although further data from the last years of HERA I are available for analysis, the improvement in statistics is expected to be only a factor of 2-3, due to the trigger downscales that were necessary to maintain acceptable rates. Using the VFPS to trigger this channel will be highly beneficial, due to the cancellations of systematics when comparing with parton densities extracted from the F_2^D as measured using the VFPS. For HERA II, it is expected that this channel can be triggered with up to 80% efficiency by using the Fast Track Trigger to reconstruct the D^* meson [7]. However, the additional use of the VFPS will clearly improve the efficiency and its associated systematics and will allow relaxed trigger conditions for the D^*.

Fig. 18 illustrates the acceptance of the VFPS and the FPS for D^* production in the kinematic region $x_{I\!P} < 0.04$, $|t| < 1$ GeV^2, $0.005 < y < 0.7$ (as covered in [17]) and $8 < Q^2 < 100$ GeV^2 (as will be available with the modified SPACAL). The data are kinematically restricted to relatively large $M_{\rm X}$ due to the charm threshold, and thus appear dominantly at large $x_{I\!P}$. Thus, even allowing for the coasting beam restriction, approximately half of all D^* events observable in H1 give rise to leading protons in the VFPS. By contrast, due to the lower overall acceptance, only a small fraction of diffractive D^* events are observable in the FPS.

Using the RAPGAP model, we estimate that a sample of 380 (310) $D^* \rightarrow K\pi\pi_{\rm slow}$ events will be obtained in a VFPS sample of 350 pb$^-1$ without (with) corrections for the coasting beam. With these statistics, it will be possible to determine whether the anomalously small cross section measured in [17] is a statistical fluctuation, or whether it represents a breakdown of diffractive factorisation. Differential measurements will also be possible, allowing us to distinguish between alternative dynamical models.

5.5.2 Diffractive Dijet Electroproduction

Diffractive dijet production does not suffer from quite the same statistical limitations as diffractive charm production, since there are no large factors due to branching ratios to observable channels. A recent H1 measurement [18] using data from 1996 and 1997 was based on a sample of approximately 2500 events. These statistics will improve by using more recent data, though higher E_t thresholds to avoid downscaling in the later stages of the trigger will restrict

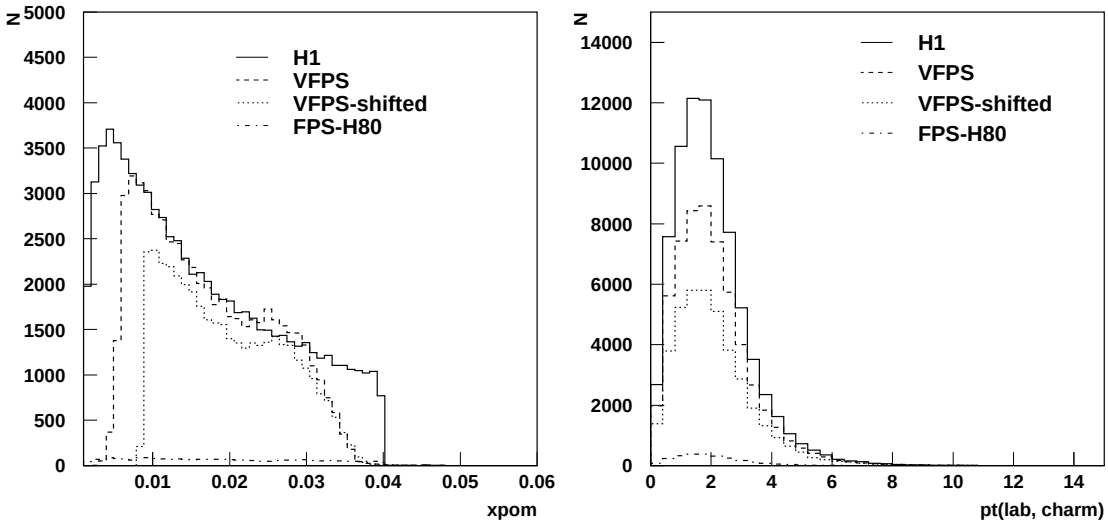

Figure 18: $x_{I\!P}$ and $p_{\rm T}$ distributions of charm electroproduction events observable in H1. The full lines show the distributions for the full H1 central detector acceptance. The subsets of events tagged by the VFPS at 12σ from the beam, tagged by the VFPS at 12σ+3 mm from the beam and tagged by the FPS are also shown. The overall normalisation is arbitrary.

the phase space available for the analysis. Despite the large global sample, statistics remain poor in regions of particular interest. For example, the *exclusive* production of dijets (i.e the case where the X system contains only a pair of jets) has a very small cross section, but is believed to be fully calculable in perturbative QCD [16]. Final states containing 3 high $p_{\rm T}$ jets are also of special interest, since diffractive final states are often modelled as $q\bar{q}g$ systems. The analysis of three-jet production in [18] was based on only 130 events.

Fig. 19 illustrates the VFPS acceptance for dijets in the kinematic range covered in [18], further restricted to $Q^2 > 8\ {\rm GeV}^2$. The kinematic restriction to high $x_{I\!P}$ imposed by the jet requirements is even more pronounced here than for the charm case, with almost no loss of acceptance at low $x_{I\!P}$ due to the coasting beam. Almost all dijet events with $x_{I\!P} < 0.03$ yield protons in the VFPS. Again this contrasts dramatically with the situation for the FPS. Using the RAPGAP Monte Carlo model, we estimate that a VFPS sample of $350\ {\rm pb}^{-1}$ will contain 22900 (20900) measurable diffractive dijet events without (with) the coasting beam restriction.

5.5.3 Diffractive Dijet Photoproduction

The study of diffractive dijet photoproduction was discussed in [1]. This channel provides an important control experiment in attempting to understand the relationship between diffractive DIS at HERA and diffractive $p\bar{p}$ scattering, for instance at the Tevatron. At present, hard diffractive scattering rates at the Tevatron fall short of predictions based on parton densities extracted from $F_2^{D(3)}$ at HERA [19] by around an order of magnitude. This failure of diffractive hard scattering factorisation is usually interpreted in terms of secondary scattering effects in processes

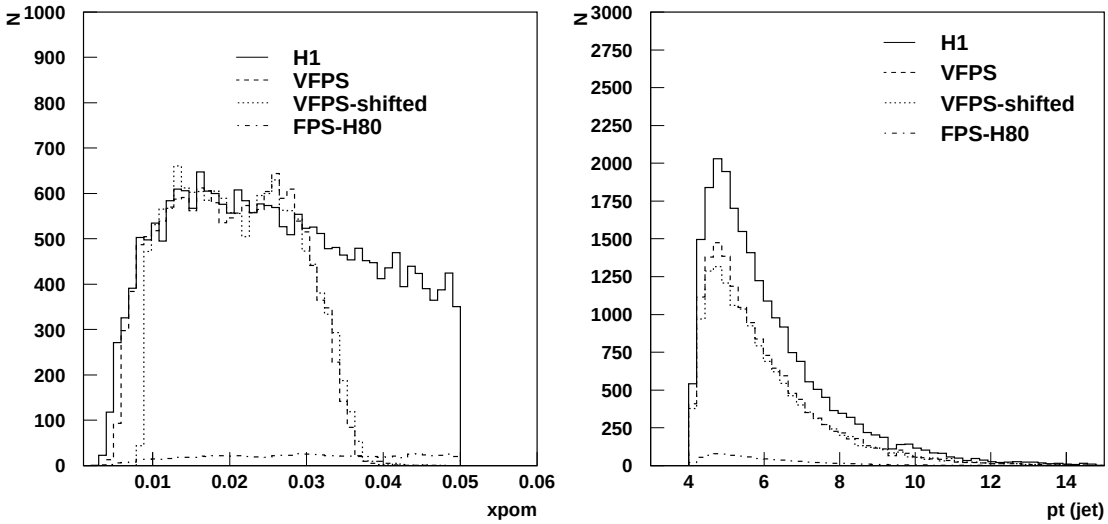

Figure 19: $x_{I\!P}$ and $p_{\rm T}$ distributions of dijet electroproduction events observable in H1. The full lines show the distributions for the full H1 central detector acceptance. The subsets of events tagged by the VFPS at 12σ from the beam, tagged by the VFPS at 12σ+3 mm from the beam and tagged by the FPS are also shown. The overall normalisation is arbitrary.

where hadronic remnants exist, leading to 'Rapidity gap survival probabilities' lower than unity. Specific phenomenological models of rapidity gap destruction effects [20, 21] are able to reproduce the factor of 10 discrepancy, though the intrinsically non-perturbative nature of the effect implies that such models have large uncertainties. An important control experiment is available in diffractive dijet photoproduction, where relatively large rates are expected both where there is no hadronic remnant of the photon (direct photoproduction) and where a hadronic remnant exists (resolved photoproduction). Early HERA data [22] suggest that the rapidity gap survival probability for resolved photoproduction is much larger than that for $p\bar{p}$ data at higher centre of mass energy.

For HERA II, H1 will have two low angle electron taggers. The 6 m tagger will cover the region $0.7 \lesssim y \lesssim 0.8$ with acceptance close to 100%, whereas the 40 m tagger will cover the region $0.1 \lesssim y \lesssim 0.3$ with acceptance varying between 25% and 80%, depending on y and on whether e^+ or e^- beams are in use. Data from the 6 m tagger will be used to obtain photoproduction cross sections at a γp centre of mass energy $W \sim 275$ GeV. The 40 m tagger will yield results at $W \sim 140$ GeV.

The RAPGAP Monte Carlo model has been used to simulate diffractive dijet photoproduction using parton distributions extracted from F_2^D, without corrections for rapidity gap destruction effects. Using the 6 m tagger to detect the outgoing electron, the central detectors to reconstruct jets with transverse energies above 5 GeV and the VFPS to tag the leading proton, we expect to collect a sample of around 1400 events from HERA II. Using the 40 m tagger, we anticipate a sample of approximately 20000 events. As for the case of dijet electroproduction, these yields are largely insensitive to the positioning of the detector relative to the beam, such

that the coasting beam is not an issue. The high precision expected with these event yields, the factor of two difference in centre of mass energy between the measurements in the two taggers and the correspondingly different fractions of direct and resolved photoproduction processes should provide an extremely useful tool for distinguishing between different models and understanding rapidity gap destruction effects.

5.6 Measurements of Azimuthal Asymmetries

The ability of the VFPS to measure the azimuthal angle ϕ of the scattered proton leads to exciting possibilities of separately evaluating longitudinally and transversely polarised photon induced diffractive cross sections. This could lead to the considerable progress in the understanding of diffractive DIS, as discussed in [1].

The relative angle $\Delta\phi$ is defined as the azimuthal angle between the electron scattering plane and and the proton scattering plane. Since the precision on the electron ϕ obtained from the SPACAL calorimeter is extremely good, the precision with which $\Delta\phi$ can be measured is entirely determined by the VFPS.

For unpolarised electrons and protons, the cross section for $ep \to epX$ can be generally written in terms of $\Delta\phi$, the cross sections for longitudinally (σ_L) and transversely (σ_T) polarized photons and their interferences as

$$\frac{d\sigma^D}{d\Delta\phi} \propto \sigma_T + \sigma_L - 2\sqrt{\epsilon(1+\epsilon)}\sigma_{LT}\cos\Delta\phi - \epsilon\sigma_{TT}\cos 2\Delta\phi \quad (2)$$

$$\frac{d\sigma^D}{d\Delta\phi} \propto 1 + A_{LT}\cos\Delta\phi \quad (3)$$

where σ_{LT} and σ_{TT} are the interference terms between the longitudinal and transverse contributions and between the two different transversely polarized photon contributions respectively and the polarisation parameter ϵ is a known function of y only, close to unity throughout most of the measurable kinematic region at HERA. The measurement of the $\Delta\phi$ dependence of the cross section thus provides information on the interference terms, which are otherwise not accessible.

A first study of the $\Delta\phi$ asymmetry integrated over the region $4 < Q^2 < 100\ \mathrm{GeV}^2$, $x_{I\!P} < 0.03$, $M_{\mathrm{X}} > 1.5\ \mathrm{GeV}$ and $0.0075 < |t| < 0.35\ \mathrm{GeV}^2$ using the ZEUS LPS [13] led to the result $A_{LT} = -0.049 \pm 0.058\ (\mathrm{stat})^{+0.056}_{-0.009}\ (\mathrm{syst})$, which is compatible with zero. As shown in fig. 10, the VFPS resolution in ϕ is expected to be approximately 0.4 radians for $|t| \gtrsim 0.2\ \mathrm{GeV}^2$, allowing measurements to be made in around 15 bins. It was shown in section 5.4 that for a luminosity of $350\ \mathrm{pb}^{-1}$, around 10000 events could be expected in each of these bins, such that the measurement will certainly be systematically limited. With this level of statistics, it will also be possible to perform the study in separate bins of β and Q^2. Strong variations with these variables are expected, with the higher twist longitudinal photon induced cross section expected to be dominant at large β and small Q^2 [10, 23]. It may also be possible to make separate studies for exclusive channels such as dijet production, where there are definite predictions for the longitudinal contribution [16].

Using the full beam and acceptance simulation of the VFPS, we have made preliminary studies of the sensitivity to asymmetries in the $\Delta\phi$ distribution. The smearing induced by the finite resolutions tends to modify the asymmetry by up to a factor of 2, though full studies of unfolding procedures and systematic uncertainties have yet to be performed.

5.7 Exclusive Channels

The acceptance regions of the VFPS for vector meson production were shown in [2]. Here, we briefly discuss the possibilities for studying the Deeply Virtual Compton Scattering (DVCS), i.e. the hard diffractive scattering of a virtual photon off a proton: $e^+p \to e^+\gamma p$ with the VFPS. This is one of the most promising diffractive channels to be studied at HERA II. The interest of this process resides in the particular insight it gives for the relevance and applicability of perturbative QCD in the field of diffractive interactions. Compared to vector meson production, DVCS is theoretically simpler because the composite meson in the final state is replaced by the photon, thus avoiding large uncertainties due to the unknown meson wave functions. Moreover, a considerable motivation comes from the access the DVCS process gives to a new class of parton distribution functions, the skewed parton distributions (SPD) which are generalisations of the familiar parton distributions of deep inelastic scattering, but include parton momentum correlations. A first cross section measurement has been achieved by H1 (based on about 100 DVCS events collected in 1997) as a function of the photon virtuality, Q^2, and the invariant mass of the final state $\gamma - p$ system, W, in the kinematic range $2 < Q^2 < 20\,\mathrm{GeV}^2$, $30 < W < 120\,\mathrm{GeV}$ [24].

For HERA II, the inner SpaCal has been removed restricting the acceptance for Q^2 below 8 GeV^2, though some acceptance remains down to $Q^2 \sim 2\,\mathrm{GeV}^2$. As has been shown in section 4, the trigger rate is such that an inclusive SpaCal trigger would have to be downscaled. Assuming a Q^2 dependent downscaling scheme that achieves a maximum trigger rate of 1 Hz, the expected number of events that will be triggered by the simple SPACAL trigger for the full period of HERA II has been calculated. The results are shown in column 3 of tables 2 and 3. Assuming that an identical trigger with the additional requirement of a VFPS signal would operate without any downscaling, DVCS events in the restricted kinematic range covered by the VFPS can be triggered with a much enhanced efficiency. Column 4 of table 2 shows the number of events that would be expected from the VFPS trigger assuming that there are no complications from the coasting beam. Column 4 of table 3 shows the same thing for the scenario where the VFPS detectors are placed an additional 3 mm from the beam in order to accommodate the coasting beam. The final columns of tables 2 and 3 show the combined number of events expected from the downscaled SPACAL trigger and from the non-downscaled SPACAL $\times$ VFPS trigger, correcting for the overlap of the two triggers.

Minimum Q^2 (GeV^2)	Produced	H1-triggered	VFPS-triggered	combined
2	29900	5052	8732	12010
8	5566	2707	2046	3636
20	828	828	487	828
40	172	172	128	172

Table 2: Number of DVCS events expected at HERA II including both events with final state protons observed in the VFPS and events with no final state proton in the VFPS. It is assumed that the coasting beam is not a problem.

It is clear that the prospects for studying DVCS at HERA II are good. For comparison, the collected data in 1997 used in [24] contained only around 25 DVCS events with Q^2 above 8 GeV^2. The expected distributions in $x_{I\!P}$, W and Q^2 for events with and without protons

Minimum Q^2 (GeV^2)	Produced	H1-triggered	VFPS-triggered	combined
2	29900	5052	4783	8754
8	5566	2707	1305	3287
20	828	828	320	828
40	172	172	94	172

Table 3: Number of DVCS events expected at HERA II including both events with final state protons observed in the VFPS and events with no final state proton in the VFPS. It is assumed that the VFPS detectors are shifted by 3 mm relative to their planned position, due to the coasting beam.

in the VFPS are shown in fig. 20. The use of the VFPS trigger approximately doubles the total number of collected DVCS events and gives the largest enhancement in the low W region where the Bethe-Heitler background is smallest. This gain occurs mainly at low Q^2 where the downscaling of the non-VFPS trigger is largest.

5.8 The VFPS with Reduced Proton Beam Energy Running

It has been suggested that a running strategy for HERA II might include around $50\ \mathrm{pb}^{-1}$ taken with reduced proton beam energies. As in the case of inclusive DIS, low proton energy running is particularly interesting for the diffractive case, since it allows access to a previously unexplored kinematic region at high x and low Q^2 and since it should yield a direct determination of the longitudinal diffractive structure function F_L^D. In [25], it was shown that an extraction of $R^D = F_L^D/(F_2^D - F_L^D)$ with an uncertainty of approximately 40% and comparable statistical and systematic errors is possible with a sample of $50\ \mathrm{pb}^{-1}$ at a proton energy of 500 GeV.

At present no beam optics calculations exist that would allow us to evaluate the performance of the VFPS at reduced proton beam energies. However on general principles one may assume that the dispersion and β function will not change too much and that the emittance will increase only slightly. Therefore we estimate that the upper $x_{I\!P}$ acceptance limit will probably not be very different, but because of the slightly wider beam, it may not be possible to place the detectors quite so close to the beam, thereby increasing the lower $x_{I\!P}$ acceptance limit. Until detailed beam optics calculations become available, it is not possible to estimate the effect on the VFPS resolution.

5.9 Further Physics Motivation

The remaining physics programme discussed in [1] remains largely valid. In particular, we would still expect to be able to constrain double dissociation cross sections and the ratio of single photon dissociation ($ep \to eXp$) to double dissociation ($ep \to eXY$) as a function of the kinematic variables $x_{I\!P}$, β and Q^2 by comparing the results of VFPS analysis with rapidity gap based analysis. This represents an interesting test of Regge factorisation and reduces the systematic uncertainties on single photon dissociation measurements.

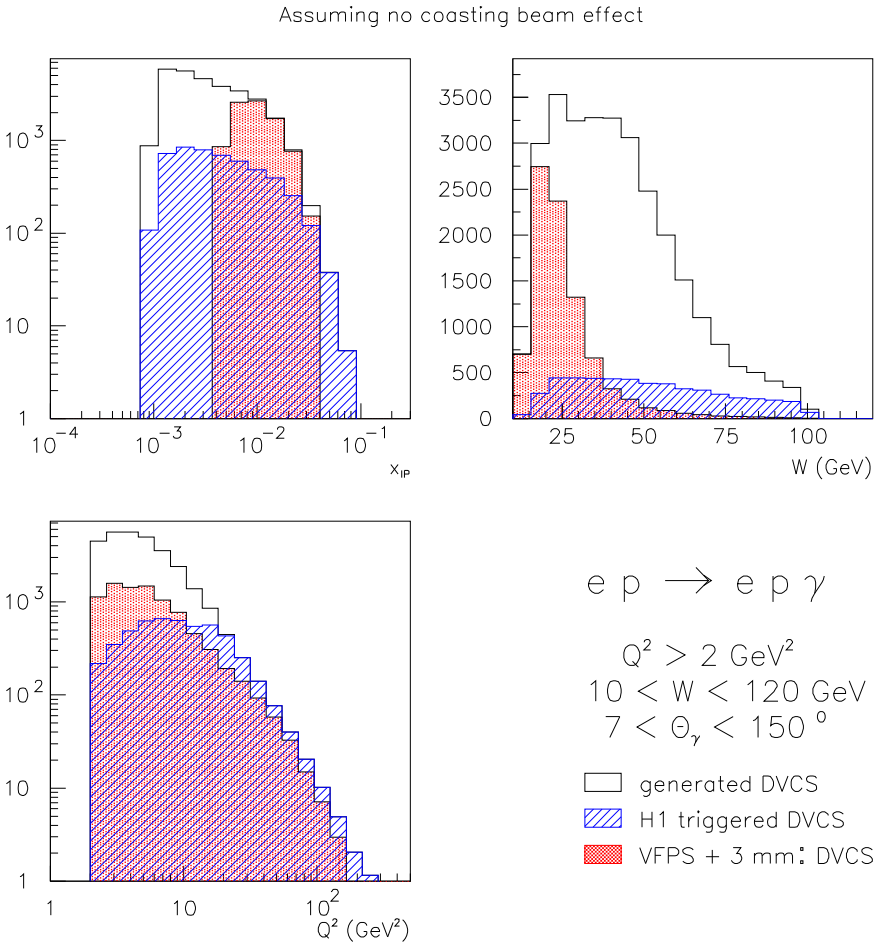

Figure 20: Expected HERA II distributions in $x_{I\!P}$, W and Q^2 for simulated DVCS events. The distributions are shown for the case where there is no coasting beam problem, separately for the full simulated sample, for events triggered using the SPACAL trigger only with Q^2 dependent downscaling to achieve a trigger rate of 1 Hz and for events triggered by the VFPS.

6 Technical Status Report

Below, we briefly summarise the present status of the VFPS project from a technical point of view.

6.1 Status of Bypass - Warm beamline - Installation

The design of the “Cold bypass” was finished in October 2001. The full design including the part drawings are ready for delivery to the construction firm, who were previously informed about the status of the bypass in June. The agreement between Brussels-DESY-Damker& Partner (design firm) and DEMACO (construction firm) has to be established. The firm Damker& Partner is presently working on the beam line support structure for the cold bypass and on the Roman pots. The installation procedure for the bypass in the tunnel remains to be worked out.

6.2 Status of Roman pot

Earlier this year the DESY machine and vacuum groups raised concerns about vacuum problems in the cold section of the beam line, which might occur if the full beam accidentally hit the base of the Roman pot detector, e.g. in the event of a sudden magnet failure. This scenario has since been studied. The energy deposited and the associated temperature rise has been simulated with GEANT and the report [26] has been sent to the DESY machine group. On October 8, 2001 the machine groups concluded that the VFPS Roman pot could be built according to the FPS drawing without further modification.

6.3 Status of detector

Scintillating fibre detectors were produced at the beginning of 2001. Placement of the detectors in the Roman pots was delayed whilst the simulations described in section 6.2 were performed. The production can now proceed.

6.4 Status of detector electronics

The detector electronics are similar to the FPS electronics. Some of the electronic boards had to be reproduced (crate controller, master controller), whilst others had to be redesigned (pipeline boards, trigger board). All design work has been completed and series production can be started.

6.5 Status of Stage (Roman pot) mover control

The FPS Roman pot mover control will be adapted such that it can be integrated into the new H1 PVSS slow control system. This will require rewriting of the motor control software but implementation in the new system will facilitate many of the control tasks.

6.6 Status of Data Acquisition

The VFPS DAQ can easily be implemented as an extension of the existing FPS DAQ. The same readout hardware will be used.

6.7 Status of Monte Carlo beamline and Roman Pot simulation

The coding of the geometry of the VFPS Roman pots in the H1 simulation code will be finalised by the end of October. The proton beam line simulation in H1SIM has started. The results of this full H1SIM beam line simulation and Roman pots can then be cross checked with the beam transport calculation.

7 Summary and Conclusions

To pursue and expand the diffractive physics results of the HERA I program into the HERA II phase, the installation of the VFPS, a very forward proton spectrometer, is highly desirable, not only for the improvements in measurement quality that it will yield, but also to provide the necessary trigger to allow high statistics samples to be collected. The physics program, described on our first proposal, has been extended in the present addendum.

To fully evaluate the physics case, we have finalised a detailed description of the proton beam line, essential in understanding the performance of the VFPS, determined the acceptance for various processes and evaluated the resolutions on the physics parameters that can be obtained from this device. This new beam transport calculation has shown that the reconstruction of these physics parameters is more complicated than was previously thought from first studies using a linear beam optics approximation. However, the newly obtained resolutions do not significantly impede the physics program.

At the technical level, one of the most important and technically complicated issues in the VFPS installation is the cold bypass. Its complete design is finished and construction can start. At present all other components can be delivered in time for installation at the end of 2002. Further delays in approval at this point could result in a failure to implement the device at that time. We would therefore ask for a full approval of the project.

References

[1] H1 VFPS Group, L. Favart et al., *Proposal for Installation of a Very Forward Proton Spectrometer in H1 after 2000*, DESY PRC 01/00.

[2] H1 VFPS Group, L. Favart et al., *Addendum VFPS: Acceptances*, addendum to DESY PRC 01/00.

[3] H1 VFPS Group, L. Favart et al., *Addendum VFPS: Background Rates*, addendum to DESY PRC 01/00.

[4] P. Van Mechelen, *Unfolding experimental distributions*, H1 note 10/96-496.

[5] H1 Collaboration, *Measurement of Semi-Inclusive Diffractive Deep Inelastic Scattering with a Leading Proton at HERA*, paper 809 submitted to EPS 2001, Budapest.

[6] H1 Collaboration, *Proposal to Upgrade the LAr Trigger: The Jet Trigger*, DESY PRC 99/02.

[7] H1 Fast Track Trigger Group, *A Fast Track Trigger with High Resolution for H1*, DESY PRC 99/06 and addendum, DESY PRC 99/07.

[8] P. Newman, *A Study of the Dynamics of Diffractive Photoproduction at HERA*, Ph. D. thesis (University of Birmingham), RAL-TH-96-011.

[9] J. Collins, Phys. Rev. D**57** (1998), 3051 and erratum ibid. D**61** (2000) 019902.

[10] K. Golec-Biernat, M. Wüsthoff, Phys. Rev. D**59** (1999), 014017;
K. Golec-Biernat, M. Wüsthoff, Phys. Rev. D**60** (1999), 114023.

[11] A. Donnachie, P. Landshoff, Phys. Lett. B**296** (1992) 227;
K. Goulianos, Phys. Rep. **101** (1983) 169.

[12] H1 Collaboration, *Measurement of the Diffractive Structure Function $F_2^{D(3)}$ at HERA*, paper 808 submitted to EPS 2001, Budapest.

[13] ZEUS Collaboration, *Results on inclusive Diffraction with the ZEUS Leading Proton Spectromenter at HERA*, paper 566 submitted to EPS 2001, Budapest.

[14] H1 Collaboration, Eur. Phys. J. C**21** (2001) 33

[15] H. Jung, *Comp. Phys. Commun.* **86**(1995) 147.
(see also http://www.desy.de/ jung/rapgap.html)

[16] J. Bartels, H. Lotter, M. Wüsthoff, Phys. Lett. B**379** (1996), 239;
J. Bartels, C. Ewerz, H. Lotter, M. Wüsthoff, Phys. Lett. B**386** (1996), 389;
J. Bartels, H. Jung, M. Wüsthoff, Eur. Phys. J. C**11** (1999), 111.

[17] H1 Collaboration, C. Adloff et al., Phys. Lett. B**520** (2001) 191.

[18] H1 Collaboration, C. Adloff et al., *Eur. Phys. J.* **C**20(2001)29-49

[19] CDF Collaboration., Phys. Rev. Lett. **84** (2000), 5043.

[20] A. Kaidalov, V. Khoze, A. Martin, M. Ryskin, Eur. Phys. J. C**21** (2001) 521.

[21] B. Cox, J. Forshaw, L. Lönnblad, JHEP **9910** (1999) 023, hep-ph/9908464.

[22] H1 Collaboration, Eur. Phys. J C**6** (1999), 421.

[23] J. Bartels, J. Ellis, H. Kowalski, M. Wüsthoff, Eur. Phys. J. C**7** (1999), 443.

[24] H1 Collaboration, C. Adloff et al., Phys.Lett. B**517** (2001) 47

[25] A. Mehta, J. Phillips, B. Waugh, *'Future Physics at HERA'* workshop, 1995/96, ed. Ingelman, de Roeck, Klanner, page 704.

[26] *Heat Deposition in the base plate of VFPS Roman pot.*, (see http://web.iihe.ac.be/h1pot/)